Astronomy & Astrophysics manuscript no. printerTVerdugo
September 22, 2014
© ESO 2014

arXiv:1409.2900v2 [astro-ph.CO] 18 Sep 2014

Characterizing SL2S galaxy groups using the Einstein radius ⋆, ⋆⋆

T. Verdugo[1,2], V. Motta[2], G. Foëx[2], J. E. Forero-Romero[3], R. P. Muñoz[4], R. Pello[5], M. Limousin[6,7], A. More[8], R. Cabanac[5], G. Soucail[9], J. P. Blakeslee[10], A. J. Mejía-Narváez[1,11], G. Magris[1], J. G. Fernández-Trincado[1,11,12]

[1] Centro de Investigaciones de Astronomía, Apartado Postal 264, Mérida 5101-A, Venezuela
[2] Universidad de Valparaíso, Departamento de Física y Astronomía, Avenida Gran Bretaña 1111, Valparaíso, Chile
[3] Departamento de Física, Universidad de los Andes, Cra. 1 No. 18A-10, Edificio Ip, Bogotá, Colombia
[4] Instituto de Astrofísica, Facultad de Física, Pontificia Universidad Católica de Chile, Av. Vicuña Mackenna 4860, 7820436 Macul, Santiago, Chile
[5] Laboratoire d'Astrophysique de Toulouse-Tarbes, Université de Toulouse, CNRS, 57 Avenue d'Azereix, 65 000 Tarbes, France
[6] Laboratoire d'Astrophysique de Marseille, Université de Provence, CNRS, 38 rue Frédéric Joliot-Curie, F-13388 Marseille Cedex 13, France
[7] Dark Cosmology Center, Niels Bohr Institute, University of Copenhagen, Juliane Marie Vej 30, 2100 Copenhagen, Denmark
[8] Kavli Institute for the Physics and Mathematics of the Universe (Kavli IPMU), The University of Tokyo, 5-1-5 Kashiwanoha, Kashiwa-shi, Chiba, 277-8583, Japan
[9] Université de Toulouse, UPS-Observatoire Midi-Pyrénées, IRAP, Toulouse, France
[10] Herzberg Institute of Astrophysics, National Research Council of Canada, Victoria, BC V9E 2E7, Canada
[11] Universidad de Los Andes, Posgrado de Física Fundamental, La Hechicera, Mérida, Venezuela.
[12] Institute Utinam, CNRS UMR6213, Université de Franche-Comté, OSU THETA de Franche-Comté-Bourgogne, Besançon, France

Accepted for publication

ABSTRACT

Aims. We aim to study the reliability of R_A (the distance from the arcs to the center of the lens) as a measure of the Einstein radius in galaxy groups. In addition, we want to analyze the possibility of using R_A as a proxy to characterize some properties of galaxy groups, such as luminosity (L) and richness (N).
Methods. We analyzed the Einstein radius, θ_E, in our sample of Strong Lensing Legacy Survey (SL2S) galaxy groups, and compared it with R_A, using three different approaches: 1) the velocity dispersion obtained from weak lensing assuming a singular isothermal sphere profile ($\theta_{E,I}$), 2) a strong lensing analytical method ($\theta_{E,II}$) combined with a velocity dispersion-concentration relation derived from numerical simulations designed to mimic our group sample, and 3) strong lensing modeling ($\theta_{E,III}$) of eleven groups (with four new models presented in this work) using Hubble Space Telescope (HST) and Canada-France-Hawaii Telescope (CFHT) images. Finally, R_A was analyzed as a function of redshift z to investigate possible correlations with L, N, and the richness-to-luminosity ratio (N/L).
Results. We found a correlation between θ_E and R_A, but with large scatter. We estimate $\theta_{E,I}$ = (2.2 ± 0.9) + (0.7 ± 0.2)R_A, $\theta_{E,II}$ = (0.4 ± 1.5) + (1.1 ± 0.4)R_A, and $\theta_{E,III}$ = (0.4 ± 1.5) + (0.9 ± 0.3)R_A for each method respectively. We found weak evidence of anti-correlation between R_A and z, with LogR_A = (0.58±0.06) - (0.04±0.1)z, suggesting a possible evolution of the Einstein radius with z, as reported previously by other authors. Our results also show that R_A is correlated with L and N (more luminous and richer groups have greater R_A), and a possible correlation between R_A and the N/L ratio.
Conclusions. Our analysis indicates that R_A is correlated with θ_E in our sample, making R_A useful for characterizing properties like L and N (and possibly N/L) in galaxy groups. Additionally, we present evidence suggesting that the Einstein radius evolves with z.

Key words. gravitational lensing: strong – galaxies: groups: general – galaxies: groups: individual: SL2S J08591–0345 (SA72), SL2S J08520–0343 (SA63), SL2S J09595+0218 (SA80), SL2S J10021+0211 (SA83)

1. Introduction

Since most of the galaxies in the Universe belong to galaxy groups (Eke et al. 2004), the systematic examination of this intermediate regime of the mass-spectrum (between large elliptical galaxies and clusters) will shed light on the formation and evolution of structures in the hierarchical framework. Although galaxy groups have been the subject of study from different approaches, such as optical (e.g., Wilman et al. 2005a,b; Yang et al. 2008; Knobel et al. 2009; Cucciati et al. 2010; Balogh et al. 2011; Li et al. 2012), X-ray (e.g., Helsdon & Ponman 2000a,b; Osmond & Ponman 2004; Willis et al. 2005; Finoguenov et al. 2007; Rasmussen & Ponman 2007; Sun 2012), and numerical simulations (e.g., Sommer-Larsen 2006; Romeo et al. 2008; Cui et al. 2011); the systematic investigation of such a

Send offprint requests to: verdugo@cida.ve
⋆ SL2S: Strong Lensing Legacy Survey
⋆⋆ Based on observations obtained with MegaPrime/MegaCam, a joint project of CFHT and CEA/DAPNIA, at the Canada-France-Hawaii Telescope (CFHT) which is operated by the National Research Council (NRC) of Canada, the Institut National des Sciences de l'Univers of the center National de la Recherche Scientifique (CNRS) of France, and the University of Hawaii. This work is based in part on data products produced at TERAPIX and the Canadian Astronomy Data center as part of the Canada-France-Hawaii Telescope Legacy Survey, a collaborative project of NRC and CNRS. Also based on *Hubble Space Telescope* (HST) data as well as Magellan (IMACS) and VLT (FORS 2) data.

mass regime from a lensing perspective has recently started (e.g., Mandelbaum et al. 2006; Limousin et al. 2009; More et al. 2012).

The Strong Lensing Legacy Survey (SL2S[1], Cabanac et al. 2007) selects its sample from the Canada-France-Hawaii Telescope Legacy Survey (CFHTLS)[2]. The SL2S has allowed us to find and study a large sample of group-scale lenses (More et al. 2012), as well as galaxy-scale gravitational lenses (Gavazzi et al. 2012). Some galaxy groups discovered in the SL2S have been studied in detail using different techniques (e.g., Tu et al. 2009; Limousin et al. 2009, 2010; Thanjavur et al. 2010; Verdugo et al. 2011), further highlighting the importance of SL2S. More et al. (2012) showed the first compilation of lens candidates, the SL2S-ARCS (SARCS) sample, consisting of 127 objects, with 54 systems labeled as promising lenses. The authors also present the first constraints on the average mass density profile of groups using strong lensing. One of the main goals of the SL2S is to accurately determine the characteristics of the lensing groups through various methods, for example with dynamics using spectroscopy (Muñoz et al. 2013) as well as weak lensing analysis and luminosity density maps (Foëx et al. 2013). In particular, the latter work combines lensing and optical analysis to further constrain the sample, and presents a list of the 80 most secure lens candidates. Even though most of the objects in the sample must be confirmed, these objects present a weak-lensing signal (detection at the 1σ level), and show an overdensity in their luminosity density maps (see Foëx et al. 2013, for a detailed discussion). Thus, these candidates give us the opportunity to test a wide range of astrophysical problems and to probe diverse phenomena.

For instance, Zitrin et al. (2012) analyzed the universal distribution of the Einstein radius on 10000 clusters in the SDSS, discussing the possibility of an Einstein radius evolution with redshift. These authors reported that the mean effective Einstein radius decreases between $z = 0.1$ to $z = 0.45$, and argue that such a decrease is possibly related to cluster evolution, since clusters at lower z are expected to have more concentrated mass distributions, thus they are stronger lenses. Considering only geometrical effects, they demonstrated that a profile steeper than the singular isothermal sphere (SIS) is necessary to explain the decline of ∼40%. Zitrin et al. (2012) explain the tentative increase in the Einstein radius towards $z = 0.5$ invoking an increase in the size of the critical curves, as a result of merging subclumps in clusters (e.g., Torri et al. 2004; Dalal et al. 2004; Redlich et al. 2012).

Our sample of secure lens candidates (Foëx et al. 2013) can be useful to test such an assertion, namely the θ_E evolution with redshift. Although it is clearly in a distinct mass range, our sample has a larger range in redshift and the benefit of being selected by their strong lensing features. In our analysis we assume that R_A (the distance between the more extended lensed image and the brightest lens galaxy in the group) is roughly the Einstein radius (obtained by More et al. 2012). This is justified since the Einstein radius provides a natural angular scale to describe the lensing geometry (Narayan & Bartelmann 1996); the typical angular separation of images is on the order of $2\theta_E$. However, we need to be cautious because there are some factors that could bias the comparison. For example, the sample selected by More et al. (2012) is made up of groups that display small arcs and giant arcs (see Section 4.1). For giant arcs, comparing R_A and θ_E is a rough estimation (e.g., Miralda-Escude & Babul 1995), since this kind of arc tends to appear close to the critical curve in a spherically symmetric mass distribution model (although in general lenses are elongated). On the other hand, comparing R_A and θ_E could be inaccurate for those images (which are not giant arcs) that appear, for example, along the major-axis critical curve. In this sense, it is important to note that arc radial positions could extend beyond the Einstein radius (depending on the Einstein radius definition, e.g., Puchwein & Hilbert 2009; Richard et al. 2009). Furthermore, comparison between the expected θ_E in the Lambda cold dark matter (ΛCDM) paradigm and observations may lead to different conclusions depending on the assumption of spherical or triaxial dark matter halos (e.g., Broadhurst & Barkana 2008; Oguri & Blandford 2009), and on which θ_E geometrical definition is used (see the discussion in the review of Meneghetti et al. 2013). Although from a lensing perspective galaxy groups are not as complex as galaxy clusters, some natural questions arise: Is R_A a reliable estimation for θ_E? What effect does asphericity or substructure have on such an assumption? The aim of the present work is to answer these questions and test the viability of using R_A as a proxy to characterize or even quantify some properties such as luminosity or richness in galaxy groups. As scaling relations are naturally expected (and have been observed at different redshifts) between the mass and optical properties in groups and clusters (e.g., Lin et al. 2003; Popesso et al. 2005; Becker et al. 2007; Reyes et al. 2008; Rozo et al. 2009; Andreon & Hurn 2010; Foëx et al. 2012, 2013), a correlation between R_A and these properties follows clearly because R_A scales with the mass of the halos.

Nowadays we have an extraordinary amount of data available in the search for and study of lensing galaxy groups from the Sloan Digital Sky Survey (Abazajian et al. 2003) or the CFHTLS, for example. There will be even more data with the upcoming long-term big survey projects such as LSST (LSST Dark Energy Science Collaboration 2012), the Dark Energy Survey (DES[3]), and EUCLID (Boldrin et al. 2012). Even though automated software is used to look for strong lensing candidate detection (e.g., Alard 2006; Seidel & Bartelmann 2007; Marshall et al. 2009; Sygnet et al. 2010; Maturi et al. 2013; Joseph et al. 2014; Gavazzi et al. 2014), we still lack crucial information for accurate lens modeling. For instance, the impossibility (in most cases) of spectroscopically confirming the lensing nature of arcs in groups, or even dynamically confirming that the members of the group-lensing candidates are gravitationally-bound structures (e.g., Thanjavur et al. 2010; Muñoz et al. 2013). The study presented by Foëx et al. (2013), and the present work, try to tackle this lack of spectroscopic information, by analyzing the strong-lensing group candidates using complementary approaches.

To this end, we present the Einstein radius analysis of the secure sample of galaxy groups in the SARCS sample. We consider three methods that use 1) the velocity dispersion from a weak lensing analysis, following Foëx et al. (2013); 2) strong lensing models following Broadhurst & Barkana (2008), together with numerical simulations that mimic the properties of our group sample; and 3) strong lensing modeling using a ray-tracing code (coupled with new spectroscopic data for one of the groups). Finally, we analyze the correlations between R_A and the optical properties of the groups. Our paper is arranged as follows: In Sect. 2 we present the observational data images and spectroscopy. We describe the numerical simulations in Sect. 3. In Sect. 4 we explain the methodology used to cal-

[1] http://www-sl2s.iap.fr/

[2] http://www.cfht.hawaii.edu/Science/CFHLS/

[3] http://www.darkenergysurvey.org/

Table 1: Photometric data for galaxies and arcs used in the four new gravitational lensing models.

ID	Galaxy/Arc	u^*	g'	r'	i'	z'	k_s
SL2S J08591−0345 (SA72)	G	25.4 ± 0.1	23.51 ± 0.02	21.96 ± 0.01	20.681 ± 0.004	20.245 ± 0.005	–
	A	25.0 ± 0.1	24.1 ± 0.1	23.4 ± 0.1	22.7 ± 0.1	22.4 ± 0.1	20.7 ± 0.1
SL2S J08520−0343 (SA63)	G1	23.62 ± 0.06	21.437 ± 0.009	19.808 ± 0.004	18.971 ± 0.003	18.577 ± 0.005	–
	A	27.2 ± 0.9	24.42 ± 0.07	23.39 ± 0.04	22.56 ± 0.03	22.52 ± 0.08	–
SL2S J09595+0218 (SA80)	G	25.59 ± 0.05	24.69 ± 0.02	23.098 ± 0.007	21.753 ± 0.003	20.987 ± 0.004	–
	A	25.23 ± 0.04	24.97 ± 0.03	25.20 ± 0.05	24.94 ± 0.05	24.14 ± 0.07	–
SL2S J10021+0211 (SA83)	G	25.59 ± 0.05	24.69 ± 0.02	23.098 ± 0.007	21.753 ± 0.003	20.987 ± 0.004	–
	B	25.83 ± 0.07	24.04 ± 0.01	23.42 ± 0.01	23.04 ± 0.01	22.68 ± 0.01	–

Notes. Column (1) is the identification for each object (see text). Column (2) is the object type. Columns (3-7) are the CFHTLS magnitudes. Column (8) is the magnitude in the k_s band from WIRCam.

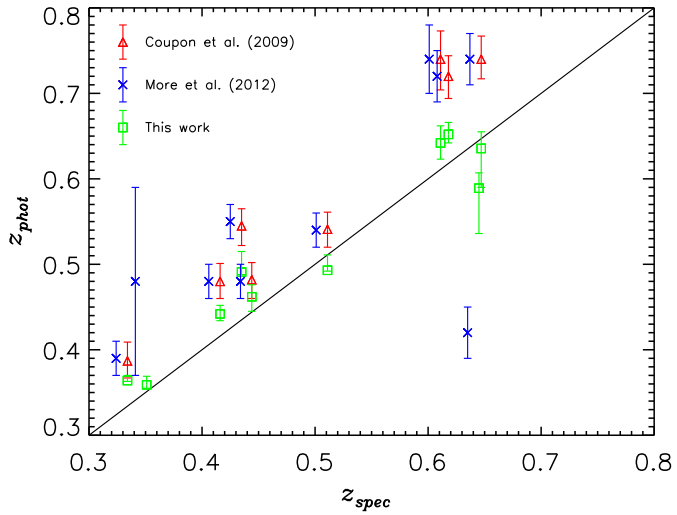

Fig. 1: Comparison between spectroscopic (from Limousin et al. 2009; Muñoz et al. 2013) and photometric redshifts. Red triangles depict the z_{phot} from Coupon et al. (2009), blue crosses the values reported in More et al. (2012), and green squares those from this work. Blue crosses were shifted in z_{spec} for clarity.

culate the Einstein radius with the three different methods. We summarize and discuss our results in Sect. 5. Finally in Sect. 6, we present the conclusions. All our results are scaled to a flat, ΛCDM cosmology with $\Omega_M = 0.3, \Omega_\Lambda = 0.7$ and a Hubble constant $H_0 = 70\ \mathrm{km\,s^{-1}\ Mpc^{-1}}$. All images are aligned with WCS coordinates, i.e., north is up, east is left. Magnitudes are given in the AB system.

2. Data

The objects presented in this work have been imaged by ground-based telescopes and in some cases by the Hubble Space Telescope (HST). From the ground, the groups were observed in five filters (u^*, g', r', i', z') as part of the CFHTLS (see Gwyn 2011) using the wide-field imager MegaPrime, which covers ∼1 square degree on the sky, with a pixel size of 0.186″. The galaxy group SL2S J08591–0345 (SA72) was observed by WIRCam (near infrared mosaic imager at CFHT) as part of the proposal 08BF08 (P.I. G. Soucail). From space, the lens was followedup with the HST in snapshot mode (C 15, P.I. Kneib) in three Advanced Camera For Surveys (ACS) filters (F814, F606, and F475). In addition, spectroscopic follow-up of the arcs in SL2S J08591–0345 (SA72) and SL2S J08520-0343 (SA63) were carried out with IMACS at Las Campanas Observatory. Throughout the present paper we will keep both names for some of the discussed lensing groups, the long name, e.g. SL2S (see Cabanac et al. 2007) because it gives us the object's coordinates, and the compact SARCS name, e.g. SA, to be consistent with More et al. (2012).

2.1. Imaging

Photometric redshifts for the group sample were reported in More et al. (2012). However, for the groups discussed in Sect. 4.3 the photometric redshifts (z_{phot}) were estimated for both the lens and the lensed galaxy. For these four lens groups we estimated their z_{phot} using the magnitudes of the brightest galaxy populating the strong lensing deflector. The photometry for these galaxies was performed in all CFHT bands with the IRAF[4] package *apphot*. Considering that the magnitudes of the lens galaxy could be contaminated by the close and bright arcs (biasing the photometric redshift), we carefully measured the magnitudes using different apertures (5,8,11,13,15, and 18 pixels). Then each aperture measurement was used to estimate redshifts using the HyperZ software (Bolzonella et al. 2000). The best redshifts were selected, i.e. those with the highest probability; using selected apertures with no contamination due to arcs or other galaxies. The photometric data and redshifts estimations are presented in Table 1 and Table 4.

The method is tested estimating photometric redshifts for some groups with reported spectroscopy (Limousin et al. 2009; Muñoz et al. 2013). These groups are SL2S J02215-0647 (SA39), SL2S J0854-0121 (SA66), SL2S J02140-0532 (SA22), SL2S J02141-0405 (SA23), SL2S J02180-0515 (SA33), SL2S J08591-0345 (SA72), SL2S J22214-0053 (SA127), SL2S J14081+5429 (SA97), SL2S J14300+5546 (SA112), and SL2S J02254-0737 (SA50). In Figure 1 we compare our z_{phot} (as well as previously reported values) with the spectroscopic red-

[4] IRAF is distributed by the National Optical Astronomy Observatory, which is operated by the Association of Universities for Research in Astronomy (AURA) under cooperative agreement with the National Science Foundation.

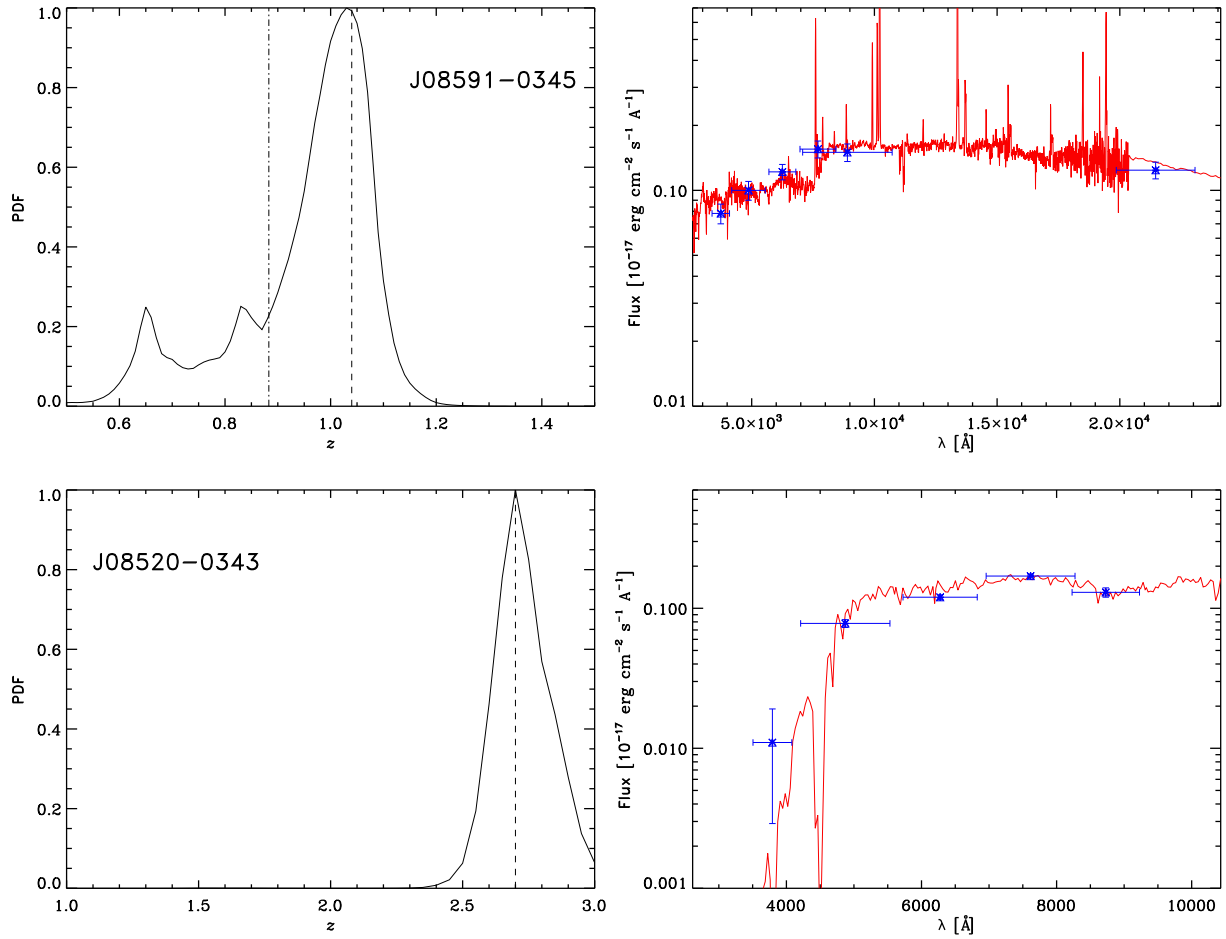

Fig. 2: *Left column.* Output photometric redshift PDF for the selected arcs (see text). The dashed vertical lines corresponds to the best redshift estimation. In SL2S J08591−0345 the dash-dotted line corresponds to the spectroscopic value. *Right column.* Best fit spectral energy distribution. Points with error bars are the observed CFHTLS broadband magnitudes and k_s from WIRCam (vertical error bars correspond to photometric errors, horizontal error bars represent the range covered by the filter).

shift. We note that the z_{phot} values from More et al. (2012) and Coupon et al. (2009) are slightly overestimated, probably because of the automatic extraction of the magnitudes used in those works.

Another effect to take into account in z_{phot} calculations is that the point-spread functions (PSF) are different for each filter band, which makes it difficult to match physical apertures. This is especially important when estimating the magnitudes of the arcs (Table 1) because the different degree of blurring in each filter band could produce an important bias in the redshift estimations (Hildebrandt et al. 2012). Thus, for the arcs, we proceed in another way.

Although photometric redshifts have been used extensively in clusters of galaxies to compute arc redshifts (e.g. Sand et al. 2005), in galaxy groups the process can be very challenging (see Verdugo et al. 2011) since the arcs are usually near the central galaxy (or galaxies) and skew the results by light contamination. In order to minimize this effect, we subtract the central galaxies in each group. Following McLeod et al. (1998), we analyzed the u, g, r, i, z, and k_s images and fitted a model convolved with a PSF (de Vaucouleurs profiles were fitted to the galaxies with synthetic PSFs). After the galaxy subtraction, we employed polygonal apertures to obtain more accurate flux measurements of the selected arcs. The vertices of the polygons for each arc were determined using the IRAF task *polymark*, and the magnitudes inside these apertures were calculated using the IRAF task *polyphot*. It is important to stress that the computed redshifts (see Table 4) for the arcs have a substantial uncertainty; the worst case is SL2S J08520−0343 (SA63) at 2-σ, $\delta z_s \sim 0.16$. In spite of this deterrent, these values are used in our strong lensing models, since these errors do not have a strong influence on the Einstein radius estimations. As we will see in Sect. 4.3, the δz_s has more weight when the lensing source is located close (in redshift) to the lens. We present the output probability distribution function (PDF) for the selected arcs in the left column of Fig. 2. In the right column we depict the best fit spectral energy distribution obtained from HyperZ where we superimposed the observed data as points with error bars. For SL2S J08591−0345 (SA72), the PDF is rather wide, which likely reflects the complexity of accurately removing the light contamination from the four galaxies that lie in the center of the lensing group (see top panel of Figure 3). Nonetheless, the spectroscopic value lies within 2-σ of the photometric redshift value.

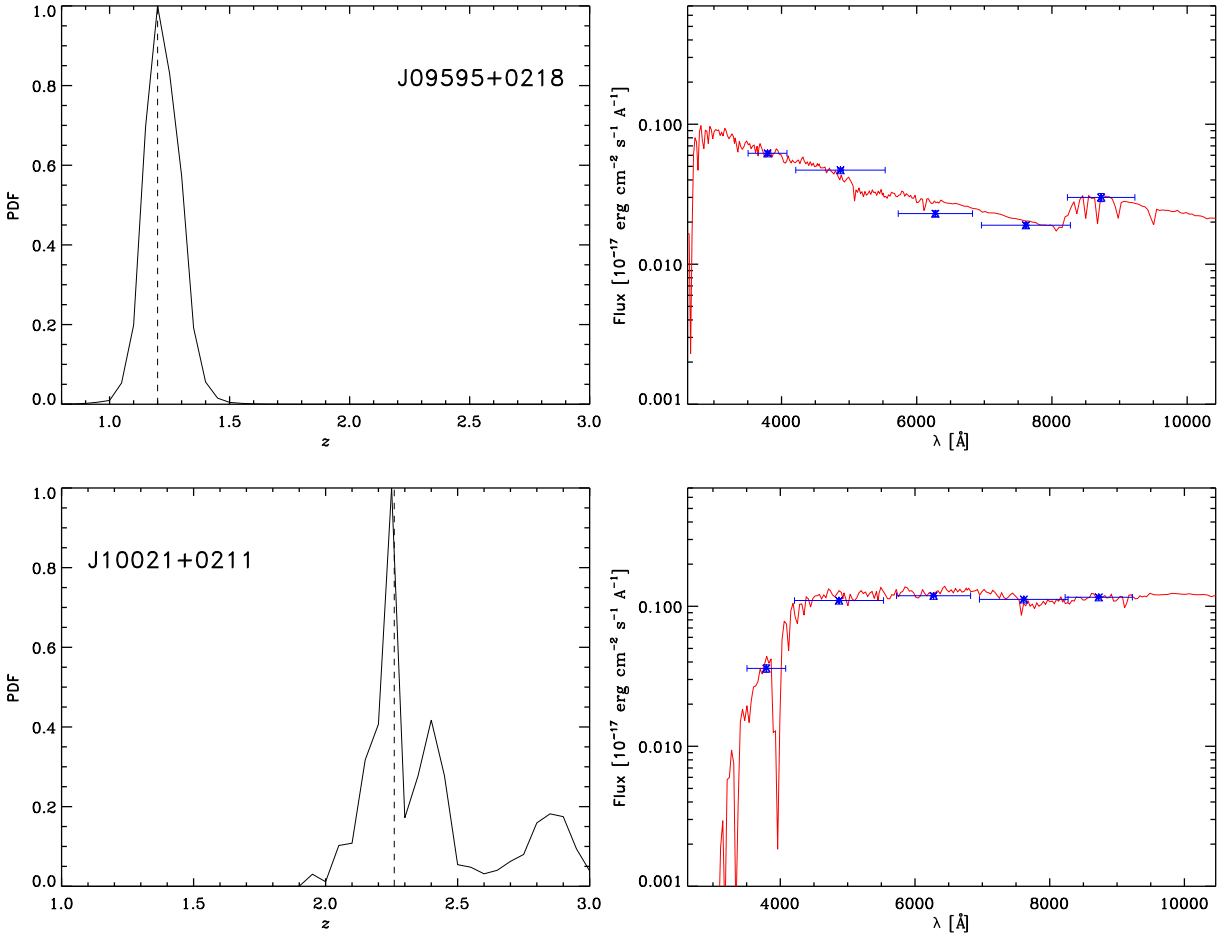

Fig. 2: Continuation. *Left column.* Output photometric redshift PDF for the selected arcs (see text). The dashed vertical lines correspond to the best redshift estimation. *Right column.* Best fit spectral energy distribution. Points with error bars are the observed CFHTLS broadband magnitudes (vertical error bars correspond to photometric errors, horizontal error bars represent the range covered by the filter).

2.2. Spectroscopy

Low resolution spectra for SL2S J08520-0343 (SA63) and SL2S J08591–0345 (SA72) were obtained with the Inamori-Magellan Areal Camera and Spectrograph (IMACS Short-Camera) at the Magellan telescope. Observations were carried out on February 19, 2012, and consisted of long-slit spectroscopy of the two systems (two exposures of 23 minutes for each target). The *grism* 200GR was used (2.037 Å/pix, 5000–9000Å wavelength range) since we were interested in the lensed source redshifts. Spectra were reduced using standard IRAF procedures consisting of dark correction, flat-fielding, and wavelength calibration (*RMS* = 0.23). Advanced steps in the data reduction consisted of a two-exposure combination to remove cosmic ray, two-dimensional sky-subtraction, and one-dimensional spectra extraction also using IRAF tasks.

The spectrum obtained for SL2S J08520-0343 (SA63) did not show any clear features (emission or absorption lines) making it impossible to obtain a redshift estimation. On the other hand, the analysis of the spectrum in one of the arcs on SL2S J08591–0345 (SA72) shows some features. We show the long slit configuration for this object, as well as the obtained spectrum in Figure 3. Some emission lines are clearly visible in the spectrum, like OIIλ3727, OIII, and H$_\beta$. Considering a starburst galaxy (Kinney et al. 1996) as comparison, we found that the spectrum is consistent with an object at $z = 0.883 \pm 0.001$. Two-dimensional spectra clearly shows OIIλ3727 and H$_\beta$ (see bottom panel of Figure 3). After applying a Gaussian fitting to those emission lines we obtain a redshift estimation of $z = 0.883 \pm 0.001$.

3. Simulations

In this section we present the characteristics of the simulation used in this work. We explain how the observational properties of our groups (More et al. 2012; Foëx et al. 2013) are used to select the dark matter halo sample that will be used in the next sections to infer the expected Einstein radii in our galaxy groups.

3.1. Simulation characteristics

We used a large N-body simulation called `Multidark` to extract statistics of halo parameters on cosmological scales. The data we use for this paper are publicly available through a database interface first presented by Riebe et al. (2011). Here we summarize

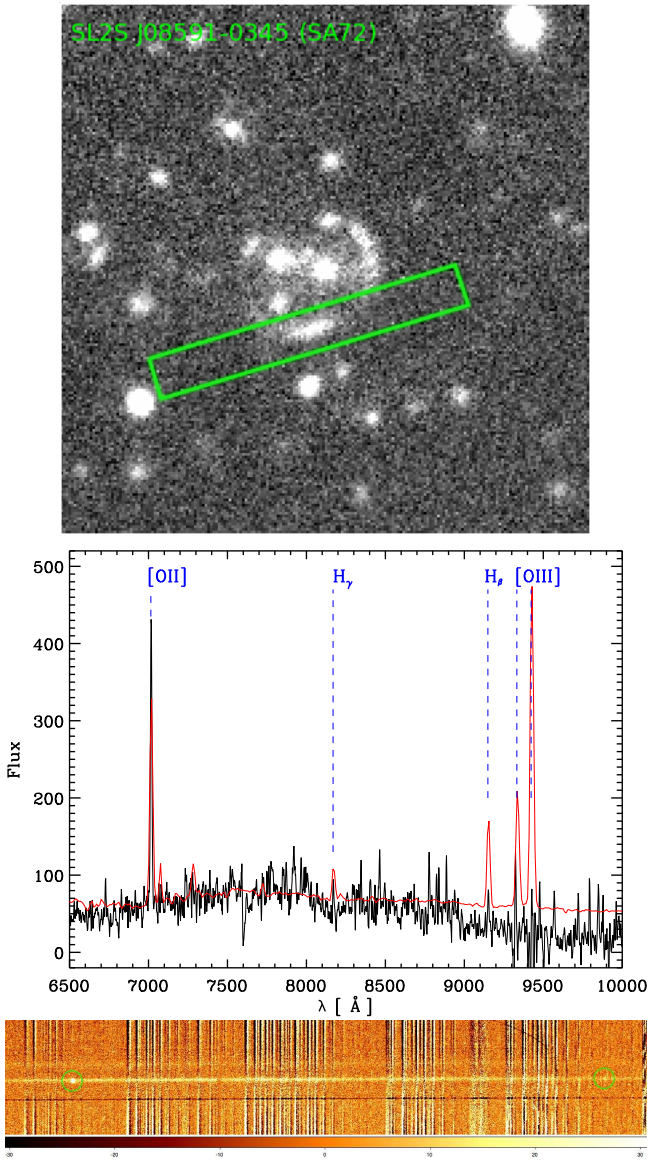

Fig. 3: *Top panel*. CFHTLS *g*-band image of SL2S J08591-0345 showing the slit position over arc A (see also second row, left panel in Figure 8). *Middle panel*. Observed spectrum of arc A (black continuous line). In red we depict a starburst template from Kinney et al. (1996) shifted at $z = 0.883$. Some emission lines are identified, e.g., [OII]λ3727, H$_\gamma$, and H$_\beta$. *Bottom panel*. Two-dimensional spectra of the same arc. We note the [OII]λ3727 and H$_\beta$ emission lines.

the main characteristics of the `Multidark` volume. More details can be found in Prada et al. (2012).

The simulation was run using an adaptive-mesh refinement code called ART. Details about the technical aspects and comparisons with other N-body codes are given in Klypin et al. (2009). The simulations follow the non-linear evolution of a dark matter density field sampled with 2048^3 particles in a volume of $1000h^{-1}$Mpc . The physical resolution of the simulation is almost constant in time $\sim 7h^{-1}$kpc between redshifts $z = 0 - 8$. The cosmological parameters in the simulation are $\Omega_m = 0.27$, $\Omega_\Lambda = 0.73$, $n_s = 0.95$, $h = 0.70$, and $\sigma_8 = 0.82$ for the matter density, dark energy density, slope of the matter fluctuations, the Hubble constant at $z = 0$ in units of 100km s^{-1} Mpc^{-1}, and the normalization of the power spectrum, respectively. These cosmological parameters are consistent with the results from WMAP5 and WMAP7 (Komatsu et al. 2009; Jarosik et al. 2011). With these characteristics the mass per simulation particle is $m_p = 8.63 \times 10^9 h^{-1}M_\odot$, which means that group-like halos of masses $\sim 10^{13} h^{-1}$M$_\odot$ are sampled with at least 1100 particles.

Table 2: Results from simulations

Center redshift bin	Simulation Snapshot	Total Number of Halos
0.05	82	781764
0.16	76	816422
0.28	70	854495
0.40	66	869768
0.52	62	901588
0.64	60	909205
0.75	56	920882
0.87	54	923512
0.99	52	904938
1.10	50	898774

Notes. Column (1) lists the center redshift bins used to query the MultiDark data base, Col. (2) the corresponding snapshot number in the simulation, Col. (3) the number of halos in the whole volume box with rms velocities in the range 300 km s^{-1}-1000 km s^{-1}.

Dark matter halos are identified using a bound-density-maxima algorithm (BDM). The code starts by finding the density maxima at the particles' positions in the simulation volume. For each maxima it finds the radius R_{200} of a sphere containing a mass over-density given by

$$M_{200} = \frac{4\pi}{3}\Delta\rho_{\rm cr}(z)R_{200}^3, \quad (1)$$

where $\rho_{\rm cr}$ is the critical density of the Universe and $\Delta = 200$ is the desired over-density. This procedure allows for the detection of both halos and subhalos. In our analysis we kept only the halos.

3.2. Concentration estimates

The estimation for the concentration values is done using an analytical property of the NFW profile (see Sect. 4.2) that relates the circular velocity at the virial radius,

$$V_{200} = \left(\frac{GM_{200}}{R_{200}}\right)^{1/2}, \quad (2)$$

with the maximum circular velocity,

$$V_{\rm max}^2 = \max\left[\frac{GM(<r)}{r}\right]. \quad (3)$$

The $V_{\rm max}/V_{200}$ velocity ratio is used to determine the halo concentration c (the ratio between R_{200} and the scale radii of the NFW profile), using the following relation (Klypin et al. 2001, 2011),

$$\frac{V_{\rm max}}{V_{200}} = \left(\frac{0.216c}{f(c)}\right)^{1/2}, \quad (4)$$

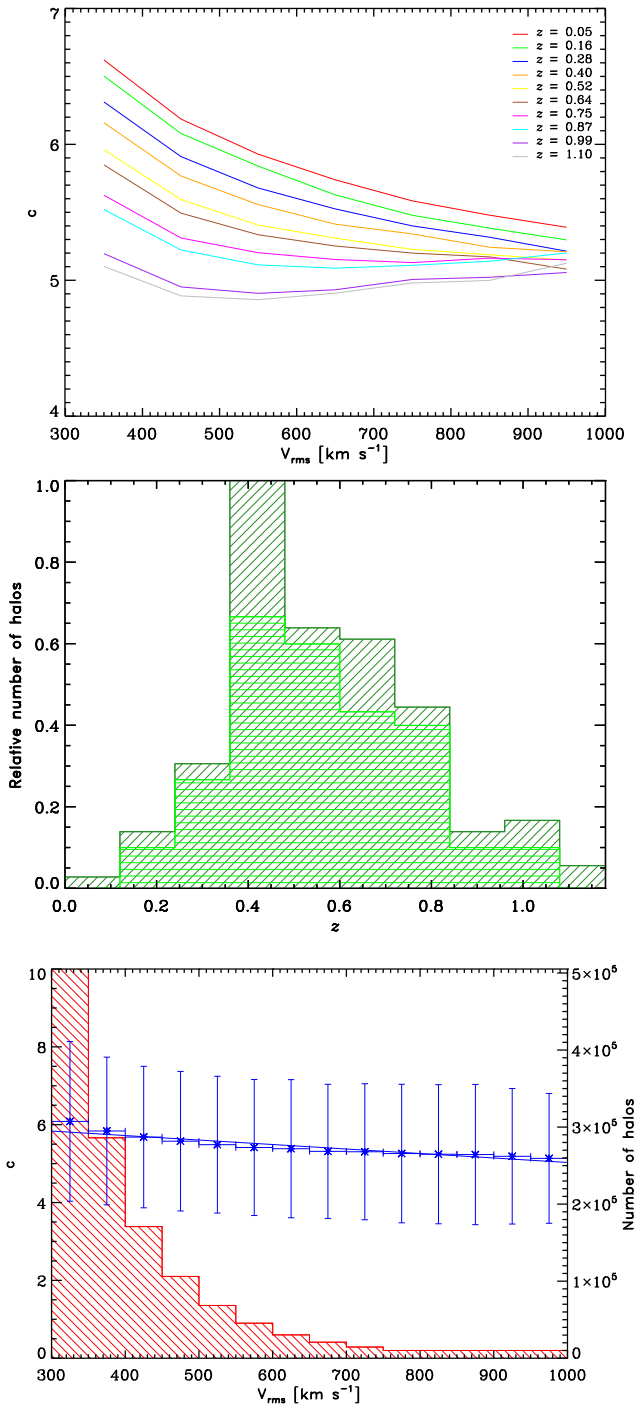

Fig. 4: *Top panel*.- $c - V_{\rm rms}$ relationship for different redshifts calculated from our simulations (see discussion in the text). *Middle panel* .- Relative number of halos calculated from the number of strong lensing groups observed in each redshift bin (according to Foëx et al. 2013). Dark green histogram with tilted lines shows the results from the whole sample, light green histogram with horizontal lines those for the secure candidates. *Bottom panel* .- $c - V_{\rm rms}$ obtained mixing, in each velocity bin, halos at different redshifts, where the relative number of halos at each redshift are equal to the observed ones, i.e., given by the fraction depicted in the middle panel. The histogram in red show the total number of halos in each velocity bin.

where $f(c)$ is

$$f(c) = \ln(1+c) - \frac{c}{(1+c)}. \quad (5)$$

For each BDM overdensity the $V_{\rm max}/V_{200}$ ratio in calculated in order to find the concentration c by solving numerically the previous two equations. This method provides a robust estimate of the concentration compared to a radial fitting to the NFW profile, which is strongly dependent on the radial range used for the fit (Klypin et al. 2011; Meneghetti & Rasia 2013). In particular, the NFW functional fit yields a small systematic offset of $(5-15)$%, and a lower concentration value when compared with the velocity ratio method (Prada et al. 2012).

3.3. Halo sample selection

We used the observational data to define ten redshift bins as given in Table 2 in order to construct a first catalog. We query the MultiDark database to obtain all the information for halos with *root mean square* velocities ($V_{\rm rms}$) in the range 300 km s^{-1}< $V_{\rm rms}$ < 1000 km s^{-1}. We use the values of $V_{\rm rms}$ as a proxy for the velocity dispersion inferred in the observed lenses (velocities were reported in Foëx et al. 2013). For each redshift we construct a relationship $c - V_{\rm rms}$ by binning the halos in the catalog in bins of 50 km s^{-1}width. For each velocity bin the average and standard deviation of the concentration is calculated (see top panel of Figure 4). We note that the concentration falls approximately in the range of $5 \lesssim c \lesssim 6$, for such intervals of redshift and velocity.

Since this range in concentration is not considerably large, we decided to test the effect of assuming a fixed value of concentration for a given velocity bin. Thus, we constructed a second halo catalog using all the halos, matching the shape of the observational redshift distribution of the lenses (More et al. 2012; Foëx et al. 2013, see middle panel of Figure 4). One of the main reasons for constructing this catalog is to have robust statistics from a single ΛCDM simulation volume, covering the mass range from groups up to clusters. Another motivation is that we will stack these objects using their velocity dispersion (Foex et al. in prep.), thus we need to know if there is any systemic difference in the estimates of θ_E when using different catalogs. We proceed as follows: for each redshift bin we count the number of observed lenses and multiply it by 10^5, then we randomly select the same number of halos from the simulation. This allows us to have a simulated sample 10^5 times larger than the observed one, with the same redshift distribution. From this new catalog we construct a new $c - V_{\rm rms}$ relationship in the same way as described above. In the bottom panel of Figure 4 we show the $c - V_{\rm rms}$ relation, using halos at different redshifts for each velocity bin, and using the same relative number of halos for each redshift as the ones that were observed. Taking into account the errors in concentration, our mimic sample has $5 \lesssim c \lesssim 6$ in the range 300 km s^{-1}< $V_{\rm rms}$ < 1000 km s^{-1}. This is consistent with the results depicted in the top panel of Figure 4. Our values are in agreement with those reported by Faltenbacher & Mathews (2007), who investigate the concentration-velocity dispersion relation in galaxy groups using cold dark matter N-body simulations.

4. Einstein radius

We calculated the Einstein radius in three different ways using 1) weak lensing, following Foëx et al. (2013) and assuming a

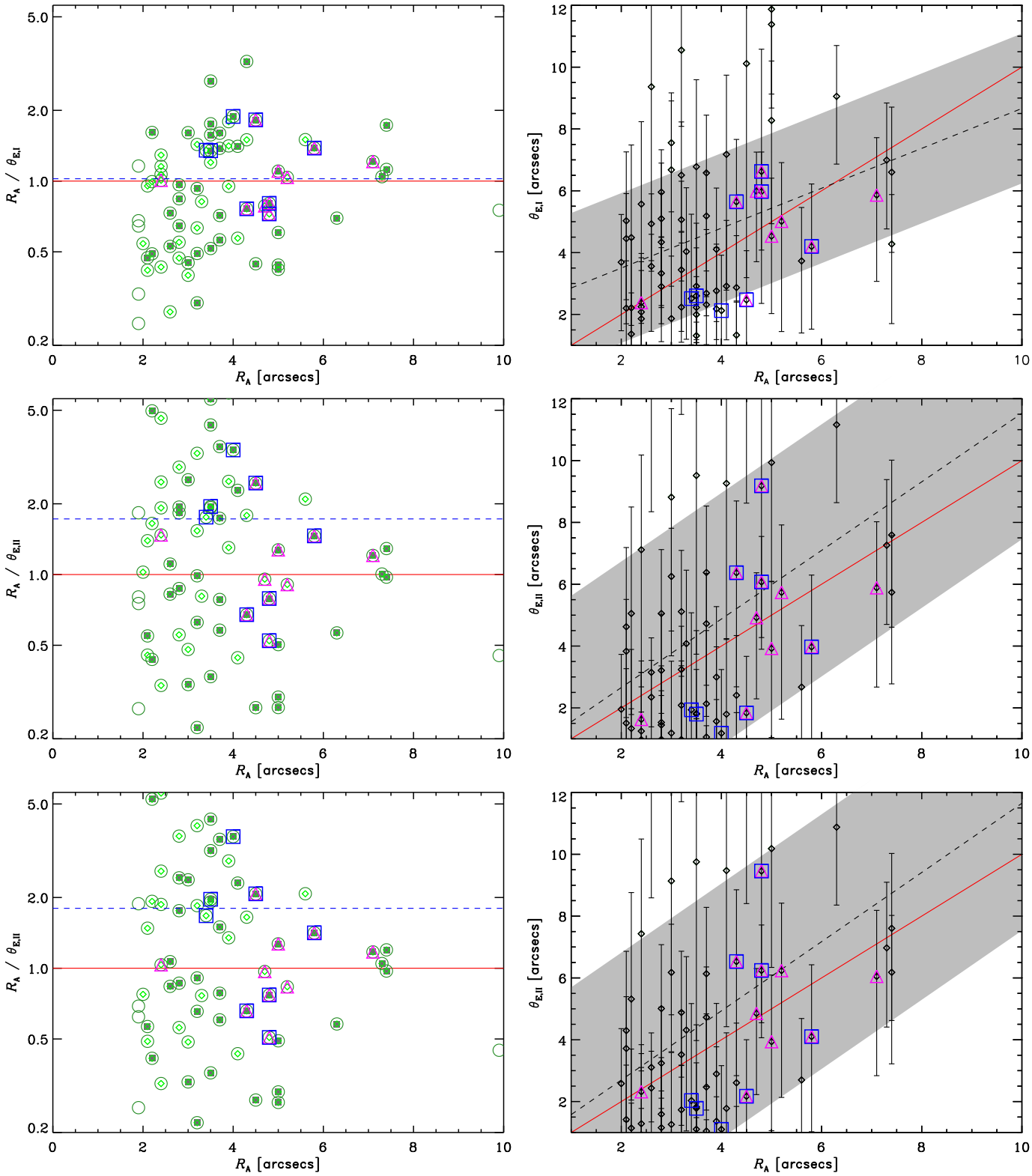

Fig. 5: *Left column.* R_A/θ_E *vs* R_A for the two first methods discussed in this work. Top panel: $R_A/\theta_{E,I}$ *vs* R_A. Green circles depict the secure group candidates (Foëx et al. 2013), green diamonds those with 2.0" $\leq R_A \leq$ 8.0". Green filled squares are groups with multi-component features or very elongated light contours (see Section 5). The blue dashed line depicts the mean $R_A/\theta_{E,I}$, the red continuous line shows the one-to-one relation, blue squares are groups with giant arcs (see Section 4.1), and magenta triangles represent those groups with strong lensing models (see Section 4.3). The error bars were omitted for clarity. Middle panel: $R_A/\theta_{E,II}$ *vs* R_A using the catalog constructed using the $V_{\rm rms}$ as proxy for the velocity dispersion measured in the observed lenses. Bottom panel: $R_A/\theta_{E,II}$ *vs* R_A using the catalog built to match the shape of the observational redshift distribution of the lenses. *Right column.* θ_E *vs* R_A. Black triangles show all the groups (regular or irregular) that satisfy 2.0" $\leq R_A \leq$ 8.0". The black dashed line shows the fit to the data, with the 1σ-error depicted as a gray shaded region. As before, the red continuous line shows the one-to-one relation.

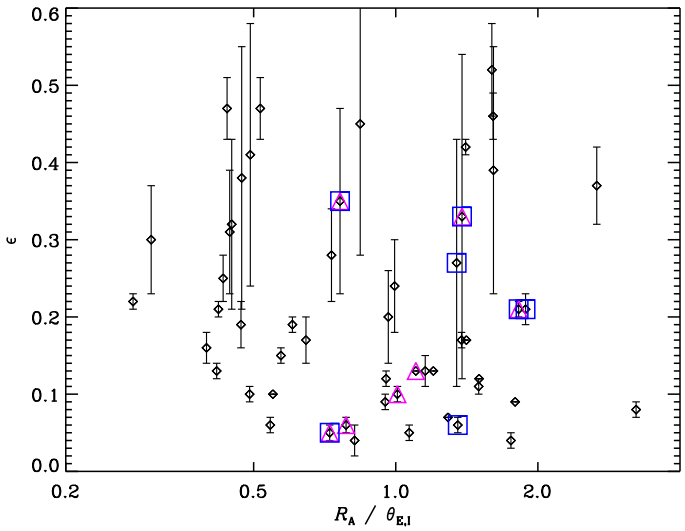

Fig. 6: The figure shows ellipticity as a function of the $R_A/\theta_{E,I}$ ratio. Blue squares are groups with giant arcs (see Section 4.1), and magenta triangles are those groups with strong lensing models (see Section 4.3).

SIS model; 2) strong lensing, considering a modified version of the method in Broadhurst & Barkana (2008) together with the $c - V_{\rm rms}$ relation obtained in the previous section; and 3) strong lensing modeling of eleven SL2S groups with HST images. The fitting is done with the LENSTOOL[5] ray-tracing code (Kneib 1993), which uses a Bayesian Markov chain Monte Carlo (MCMC) method to search for the most likely parameters in the lens modeling (Jullo et al. 2007).

4.1. Weak lensing method

The methodology used in this work follows Bardeau et al. (2007), also applied by Limousin et al. (2009) on the first SL2S group sample. A full description of the procedure can be found in Foëx et al. (2012), and of its applications in the last SL2S sample in Foëx et al. (2013). Here we outline the method briefly.

To detect and select the lensed background galaxies, we used `SExtractor` (Bertin & Arnouts 1996) on the i-band images, which computes the best seeing among all the available filters. Considering object size, its magnitude, and central flux, we perform a first selection to build separate catalogs for stars and galaxies. The shape parameters of each object are estimated using the `Im2shape` software (Bridle et al. 2002) in i-band images. Stars are used to derive the PSF field at each galaxy position, simply by taking the average shape of the five nearest stars (the catalog of stars being first cleaned to keep only objects with similar shapes). This PSF field is convolved by `Im2shape` to a given model of the galaxy shapes, in our case a simple elliptical Gaussian (see Foëx et al. 2012, 2013). Exploring the space of free parameters with a MCMC sampler, the code finds the best model that minimizes the residuals between the PSF-distorted model of the galaxy (including noise and background level, treated as well as free parameters in the modeling) to its observed shape. For each galaxy, `Im2shape` returns an estimate of its shape parameters along with robust statistical uncertainties.

[5] `This software is publicly available at: http://projets.lam.fr/projects/lenstool/wiki`

Table 3: Fitting results for θ_E vs R_A.

Correlation	a ± δ a	b ± δ b	R	P
$\theta_{E,I}$ - R_A	2.2 ± 0.9	0.7 ± 0.2	0.33	6×10^{-3}
$\theta_{E,II}$ - R_A	0.4 ± 1.5	1.1 ± 0.4	0.40	1×10^{-3}
$\theta_{E,II}$ - R_A†	0.4 ± 1.5	1.1 ± 0.4	0.40	1×10^{-3}
$\theta_{E,III}$ - R_A	0.4 ± 1.5	0.9 ± 0.3	0.60	6×10^{-2}

Notes. (†): Second catalog
Column (1) lists the correlation. Columns (2) and (3) list the coefficient values in the relation $Y = a + bX$. Columns (4) and (5) list the Spearman's rank correlation coefficient and the statistical significance, respectively.

The next step of the analysis consists in selecting the lensed galaxies to estimate the shear signal. Here we used two selections. First, we kept galaxies with $21 < m_{i'} < m_{comp} + 0.5$, i.e., we removed the brightest objects, which are most likely foreground field galaxies. We also removed the faintest ones as they are too faint to derive reliable shape parameters. By staying close to the completeness magnitude, m_{comp}, of the observed galaxy distribution, we also keep a certain control over the redshift distribution, which is required to derive the lensing strength. To remove most of the group and cluster members, we also used the classical red sequence selection: starting from the color of the central galaxy, we defined a region within the color-magnitude space where the red elliptical galaxies of the groups and clusters are located. Only galaxies outside this region were included in the catalog of the lensed galaxies.
To estimate masses from the weak-lensing signal, we computed shear profiles using the shape of the lensed galaxies. They were built with logarithmic bins centered around the lens galaxy. We fitted them with the SIS mass model within a fixed physical aperture, from 100 kpc to 2 Mpc with a classical χ^2-minimization. To propagate the uncertainties on the shear profiles $\sigma_\gamma(r)$ (intrinsic ellipticity of lensed galaxies and measurement errors on their shape parameters), we generated 1000 Monte Carlo profiles, drawn assuming that each point of the observed shear profile $\gamma(r)$ follows a normal distribution $\mathcal{N}(\gamma(r), \sigma_\gamma(r)$. The distribution of the best-fit parameters is chosen to characterize the model that best describes our observations and the associated errors (68% confidence interval around the mode of the distribution). The shear signal was translated into physical units through the lensing strength D_{LS}/D_{OS}, which was derived from the photometric redshift distributions of the CFHTLS Deep fields provided by R. Pello. The same selection criteria (magnitude limits and color-magnitude) were applied to these catalogs in order to match the redshift distribution of our lensed galaxies. In doing so, we also accounted for the dilution of the shear signal by the residual foreground galaxies (see Foëx et al. 2013, for more details).

Given the SIS velocity dispersion obtained from weak lensing, we calculate the Einstein radius through the expression

$$\theta_{E,I} = 4\pi \frac{\sigma_{WL}^2}{c^2} \frac{D_{LS}}{D_{OS}}, \quad (6)$$

where σ_{WL} is the line-of-sight velocity dispersion calculated from weak lensing data, and D_{LS} and D_{OS} are the angular diameter distances between the lens and the source and the observer

and the source, respectively. These distances are estimated using the most likely redshift of the source (Turner et al. 1984), with an upper limit given by Eq. 2 in More et al. (2011). In the top-left panel of Fig. 5 we show the ratio of $\theta_{E,I}$ calculated through Eq. 6 and their respective R_A values. The points are uniformly distributed on both sides of $R_A/\theta_{E,I} = 1$, with a mean of 1.02 and a standard deviation of 0.56 (indicating a large scatter). We also note that groups with multi-components or with a high degree of elongation (see Section 5) are also uniformly distributed in the plot. Groups with small values of $\theta_{E,I}$ with respect to R_A are always irregular. And likewise, those with extremely high $\theta_{E,I}$ values are also not regular groups. In the figure we highlight with different symbols those groups with strong lensing models (see Section 4.3) and those with giant arcs (with a length-to-width ratio larger than 10, according to More et al. 2012). We want to point out that the errors in R_A (measured directly from the images) are small compared to the errors in $\theta_{E,I}$. The former are around two pixels, which is roughly 0.4″, thus, unless otherwise specified, we will omit the error bars of R_A in the plots.

To further investigate quantitatively this effect, we use the task *ellipse* in IRAF to fit ellipses to the luminosity maps of the groups (see Foëx et al. 2013) and to obtain the ellipticity. For 14 groups it was not possible to obtain a fit because they present either multi-components or a high degree of elongation. In Fig. 6 we plot the ellipticity as a function of the ratio $R_A/\theta_{E,I}$. This result is consistent with Fig. 5 (top-left panel), i.e. elongated groups ($\epsilon > 0.3$) are evenly distributed in the $R_A/\theta_{E,I}$ axis. We note that two groups with giants arcs have $\epsilon > 0.3$, and three more do not appear in the plot (because they belong to the groups for which it was not possible to obtain a fit).

In the top-right panel of Fig. 5 we depicted $\theta_{E,I}$ vs R_A for those groups with 2.0" $\leq R_A \leq$ 8.0". In Table 3 we show the results for our fit. We found a low correlation between both variables. It is possible to show that, if we eliminate extreme values (probably outliers) in the ratio $R_A/\theta_{E,I}$, the correlation coefficient and the significance improve. For example, with a $0.5 \leq R_A/\theta_{E,I} \leq 2.0$ cutoff (following Puchwein & Hilbert 2009, who showed that around these values in the radial distribution of tangential arcs is where, approximately, the minimum and maximum in the cross-sections occurs), we found $R = 0.6$, and $P = 1{\times}10^{-5}$. However the outliers were not eliminated, keeping the sample as it is. In Section 5 we will explain the reason for such low correlation. We note that some groups with giant arcs and strong lensing models are far from the one-to-one correlation.

4.2. Analytically from a NFW profile

The NFW universal density profile, predicted in cosmological N-body simulations, has a two-parameter functional form (Navarro et al. 1997),

$$\rho(r) = \frac{\rho_{\rm cr}(z)\delta_c(z)}{(r/r_s)(1+r/r_s)^2}, \tag{7}$$

where δ_c is a characteristic density contrast, and r_s is a characteristic inner radius.

Integrating Eq. (7) and using Eq. (1), it is straightforward to show that the concentration c is related to δ_c by

$$\delta_c = \frac{200}{3}\frac{c^3}{[\ln(1+c) - c/(1+c)]}. \tag{8}$$

Then, for a given halo redshift, mass M_{200}, and concentration c, we can specify the parameters of the NFW model.

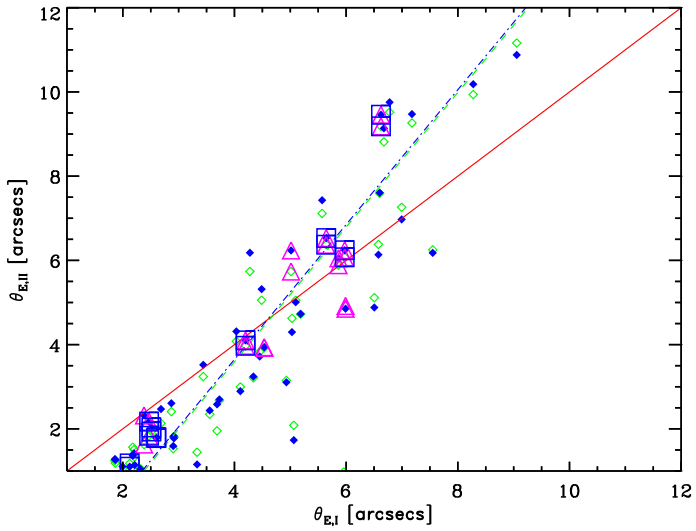

Fig. 7: $\theta_{E,II}$ *vs* $\theta_{E,I}$. Green diamonds depict the objects used to construct the plots shown in the right column (top and middle panels) of Figure 5. Green dashed line shows the fit to the data. Similarly, the blue filled diamonds are the objects associated with the correlations shown in the right column (top and bottom panels) of the same figure. Blue dash-dotted line shows the fit to the data. Blue squares are groups with giant arcs (see Section 4.1), magenta triangles are those groups with strong lensing model (see Section 4.3), and the red continuous line shows the one-to-one relation. The error bars are omitted for clarity.

We now consider a spherical NFW density profile acting like a lens. The analytical solutions for this lens were given by Bartelmann (1996), and have been studied by different authors (Wright & Brainerd 2000; Golse & Kneib 2002; Meneghetti et al. 2003). The positions of the source and the image are related through the equation

$$\boldsymbol{\beta} = \boldsymbol{\theta} - \nabla\varphi(\boldsymbol{\theta}) = \boldsymbol{\theta} - \boldsymbol{\alpha}(\boldsymbol{\theta}), \tag{9}$$

where $\boldsymbol{\theta}$ and $\boldsymbol{\beta}$ are the angular position in the image and in the source planes, respectively; $\boldsymbol{\alpha}$ is the reduced deflection angle between the image and the source; and φ is the two-dimensional lens potential. We introduce the dimensionless radial coordinate $\boldsymbol{x} = \boldsymbol{\theta}/\theta_s$, where $\theta_s = r_s/D_{OL}$, and D_{OL} is the angular diameter distance between the observer and the lens. In the case of an axially symmetric lens, the relation becomes simpler, as the position vector can be replaced by its norm.

The reduced deflection angle then becomes (Golse & Kneib 2002)

$$\boldsymbol{\alpha}(x) = \left(\frac{4\rho_{\rm cr}\delta_c r_s}{\Sigma_{cr}}\right)\frac{\theta}{x^2}g(x)\hat{e}_x, \tag{10}$$

where $g(x)$ is a function related to the surface density inside the dimensionless radius x, and is given by (Bartelmann 1996):

$$g(x) = \begin{cases} \ln\frac{x}{2} + \frac{2}{\sqrt{1-x^2}}\,\mathrm{arctanh}\sqrt{\frac{1-x}{1+x}} & \text{if } x < 1, \\ 1 + \ln\frac{1}{2} & \text{if } x = 1, \\ \ln\frac{x}{2} + \frac{2}{\sqrt{x^2-1}}\arctan\sqrt{\frac{x-1}{x+1}} & \text{if } x > 1. \end{cases} \tag{11}$$

Table 4: Summary of the strong lensing modeling.

ID	Nc	z_l	z_s	X [']	Y [']	ϵ	θ [°]	$\theta_{E,III}$ [']	R_A^a [']	rms	χ^2_{DOF}
SL2S J08591−0345 (SA72)	12	0.642±0.001*	0.883 ± 0.001	1.342 ± 0.002	-0.233 ± 0.001	0.0158 ± 0.0004	138.6 ± 0.4	4.9 ± 0.2	4.5	0.57	19
SL2S J08520−0343 (SA63)	6	$0.457^{+0.016}_{-0.016}$	2.70 ± 0.08	2.0 ± 0.1	-0.98 ± 0.04	0.30 ± 0.03	157.0 ± 0.6	5.2 ± 0.1	5.0	0.03	0.3
SL2S J09595+0218 (SA80)	4	$0.816^{+0.019}_{-0.013}$	$1.2^{+0.1}_{-0.04}$	-0.48 ± 0.04	-0.77 ± 0.05	[0.30]	[30]	2.1 ± 0.1	2.4	0.05	0.89
SL2S J10021+0211 (SA83)	2	$0.801^{+0.022}_{-0.015}$	$2.26^{+0.01}_{-0.03}$	[0]	[0]	[0.25]	[105]	3.19 ± 0.04	2.6	0.00	0.00

Notes. (*): Spectroscopic redshifts from Muñoz et al. (2013).
(a): More et al. (2012)
Columns: number of constraints Nc and optimized SIE parameters. Error bars represents 1σ confidence level on the parameters inferred from the MCMC optimization. Values in brackets are not optimized. These values correspond to models where the number of observational constraints is smaller than the number of free parameters characterizing the SIE profile. The goodness of the fit is quantified by the RMS in the image plane and the reduced χ^2_{DOF}.

The quantity $\Sigma_{crit} = (c^2/4\pi G)(D_{OS}/D_{OL}D_{LS})$ is the critical surface mass density for lensing.

If we express the deflection angle in terms of $\bar{\kappa} = (4\Sigma_{cr})\rho_{\rm cr}\delta_c r_s g(x)/x^2$, that is, the projected surface density Σ measured in units of the critical surface mass density, or, in other words, the mean enclosed surface density, then Eq. (10) can be expressed as:

$$\boldsymbol{\alpha}(x) = \bar{\kappa}\theta\hat{e_x}. \tag{12}$$

Hence, the lens Eq. (9) can be written as:

$$\boldsymbol{\beta} = \boldsymbol{\theta}\,(1 - \bar{\kappa})\,. \tag{13}$$

Following Broadhurst & Barkana (2008), we define the Einstein radius as the projected radius where the mean enclosed surface density is equal to 1. Then, for a given halo concentration parameter c, mass, halo redshift z_l, and source redshift z_s, the Einstein radius is calculated by solving the equation

$$\theta_{E,II} = \left[\frac{4\rho_{\rm cr}\delta_c r_s}{\Sigma_{cr}}\theta_s^2 g(\theta_E/\theta_s)\right]^{1/2}. \tag{14}$$

Thus, $\theta_{E,II}$ can be derived numerically using the $c - V_{\rm rms}$ relationship obtained in Sect. 3. Since we can relate $V_{\rm rms}$ to the σ_{WL} value obtained previously for each group (Sect. 4.1). Inasmuch as M_{200} is an unknown variable, we assume it is given by the mass of the isothermal profile at the projected radius R_{200}, then

$$M_{200} = \frac{\pi r_{200}\sigma^2_{WL}}{G}. \tag{15}$$

This normalization is arbitrary, but R_{200} is usually taken as a measure of the cluster's virial radius. Although there is evidence from numerical simulations that the hydrostatic assumption is valid probably within r_{500}, the kinetic pressure to thermal gas pressure ratio changes less than ≈15% between both radii (see Fig. 3 in Evrard et al. 1996). Thus, we will keep the former radius. Therefore, using Eq. (1) and Eq. (15), the scale radius in Eq. (14) is given by

$$r_s = \left[\frac{3}{4G\rho_{\rm cr}\Delta}\right]^{1/2}\frac{\sigma_{WL}}{c}. \tag{16}$$

No doubt this is an oversimplification of the problem, since we are taking the same M_{200} for both profiles, the NFW and the isothermal. This is not a good assumption, and as we will see (Section 5) it could skew the results, but it is useful to shed some light as a first-order approximation. In Fig. 5 (left column, middle and bottom panels) we show the ratio between $\theta_{E,II}$, calculated through Eq. (14), and the respective R_A for both catalogs discussed in Section 3 (the first one constructed from the $V_{\rm rms}$ as proxy for the velocity dispersion inferred in the observed lenses and the second one built to match the shape of the observational redshift distribution of the lenses). For the first case, we obtained a mean of 1.7 and a standard deviation equal to 1.6, and for the second one we obtained a mean of 1.8 with a standard deviation of 1.8, indicating a slightly larger scatter compared with the first method.

The middle- and bottom-right panels of Fig. 5 show $\theta_{E,II}$ vs R_A for the groups with 2.0" ≤ R_A ≤ 8.0". As in the first method, we found a low correlation between both variables (see Table 3). As before, if we eliminate the outliers using a $0.5 \leq R_A/\theta_{E,I} \leq 2.0$ cutoff, the results improve, and we obtain $R = 0.7$ (P =

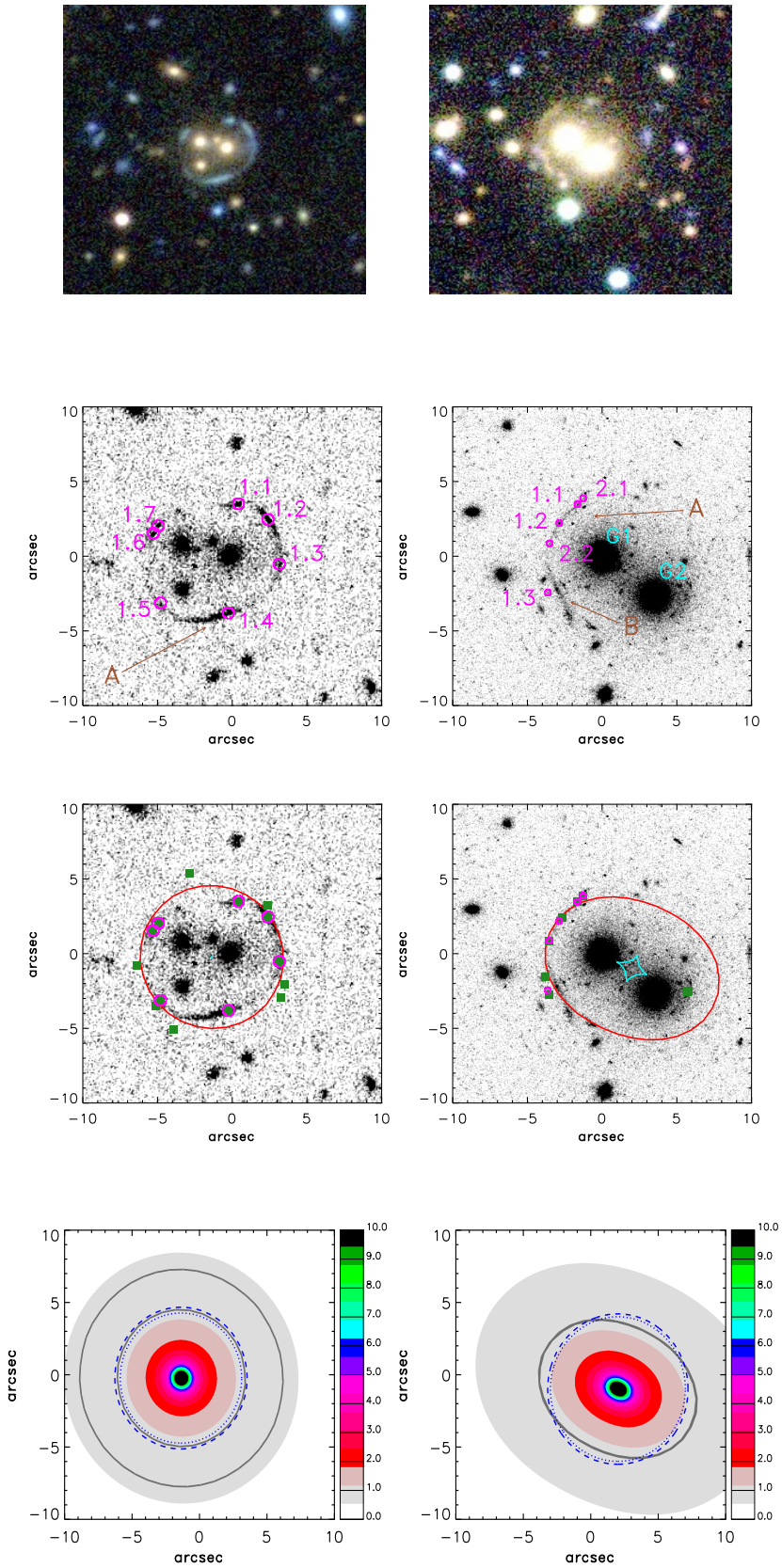

Fig. 8: SL2S J08591–0345 (SA72) and SL2S J08520–0343 (SA63), left and right columns, respectively. *First row.*- Composite CFHTLS *g*, *r*,*i* color images (30″×30″). *Second row.*- Identification of the arcs and their substructure in each lens (see Section 4.3). *Third row.*- Critical (red) and caustic lines (cyan) for the strong lensing models. The magenta circles show the measured positions of the image (input data for the model) and the green filled squares are the model-predicted image positions. *Fourth row.*- Convergence maps. For a source located at the respective redshifts, z_s, given in Table 4. Dark gray lines show $\kappa = 1$ for sources located in (z_{phot} - δz_{phot}, z_{phot} + δz_{phot}). Dotted blue lines and dashed blue lines depict the values for R_A, and $\theta_{E,III}$, respectively.

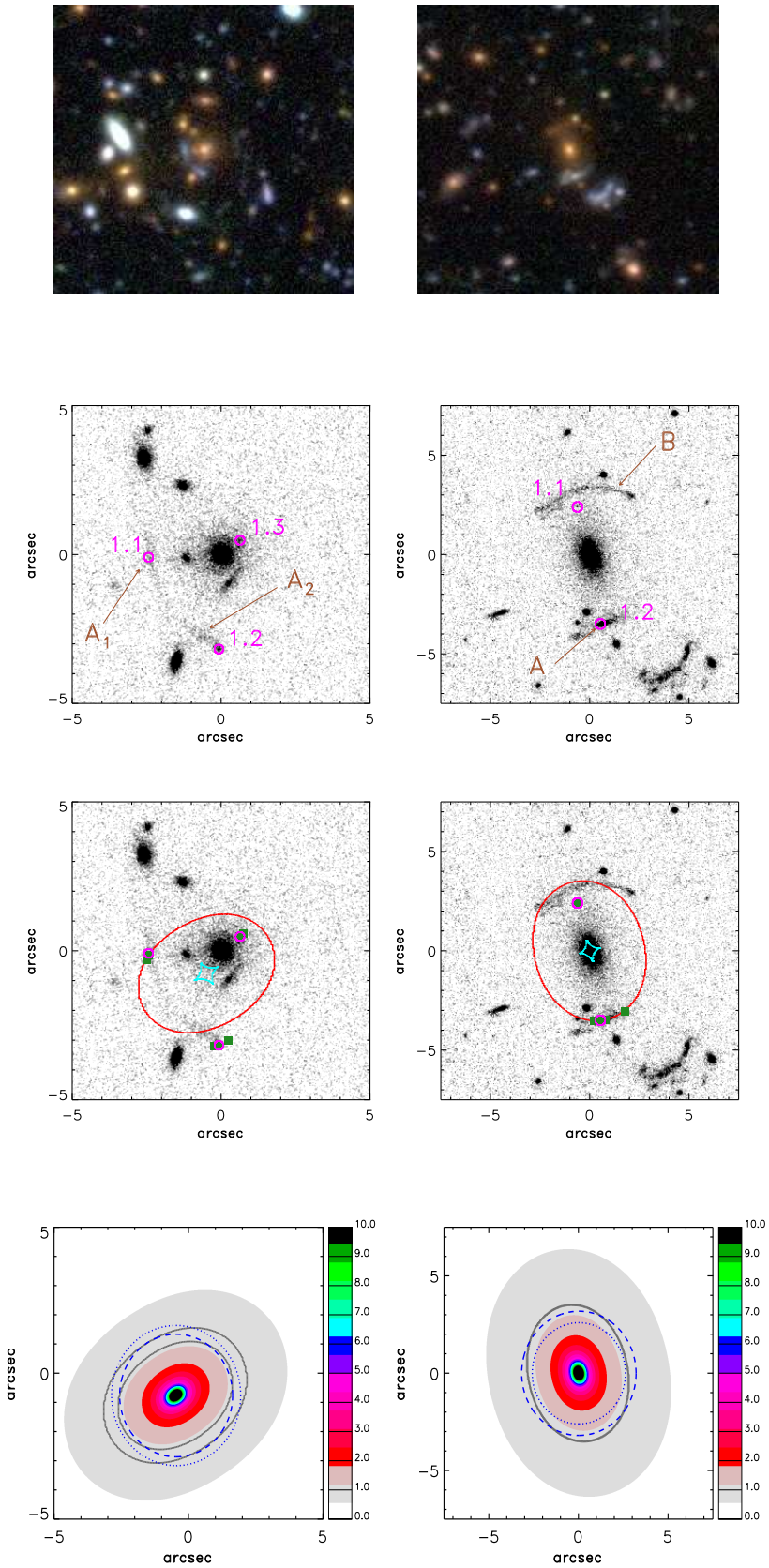

Fig. 8: Continuation. SL2S J09595+0218 (SA80) and SL2S J10021+0211 (SA83), left and right columns, respectively. *First row.*- Composite CFHTLS *g*, *r*,*i* color images (30″×30″). *Second row.*- Identification of the arcs and their substructure in each lens (see Section 4.3). *Third row.*- Critical (red) and caustic lines (cyan) for the strong lensing models. The magenta circles show the measured positions of the image (input data for the model) and the green filled squares the model-predicted image positions. *Fourth row.*- Convergence maps. For a source located at the respective redshifts, z_s, given in Table 4. Dark gray lines shows $\kappa = 1$ for sources located in (z_{phot} - δz_{phot}, z_{phot} + δz_{phot}). Dotted blue lines and dashed blue lines depict the values for R_A, and $\theta_{E,III}$, respectively.

2×10^{-7}) and $R = 0.7$ ($P = 1\times10^{-6}$) for the first and second catalog, respectively. We note again that some groups with giant arcs and strong lensing models are not close to the one-to-one correlation.

Finally, in Fig. 7 we plotted $\theta_{E,II}$ vs $\theta_{E,I}$ to look for systematic differences between both estimates. It is clear that for larger values of $\theta_{E,I}$ there is a slight overestimation of $\theta_{E,II}$. This can be explained by the large velocity dispersion calculated for the groups: the halo associated with the NFW profile needs to be more massive in order to enclose the same mass at R_{200} as the one calculated from weak lensing (WL). Similarly, the opposite is true for small values of $\theta_{E,I}$. This trend explains the change in the slopes in the correlations obtained for $\theta_{E,I}$-R_A and $\theta_{E,II}$-R_A, which is also clear in the three right panels of Fig. 5.

4.3. The ray-tracing code method

In this section, the comparison between R_A and θ_E is done using strong lensing models for 11 groups in the SARCS sample. The subsample consist of: SA22 (SL2S J02140−0532), SA39 (SL2S J02215−0647), SA50 (SL2S J02254−0737), SA66 (SL2S J08544−0121), SA112 (SL2S J14300+5546), SA123 (SL2S J22133+0048), SA127 (SL2S J22214−0053), SA72 (SL2S J08591−0345), SA63 (SL2S J08520−0343), SA80 (SL2S J09595+0218), and SA83 (SL2S J10021+0211). The first seven groups were previously modeled and the results were presented in Limousin et al. (2009). The four remaining groups were selected because they have HST images, an important asset in lensing modeling. This kind of data allows us to resolve the features in the lensed images and to improve the constraints in the models. Other reasons for their selection are that they have different characteristics (luminosity contours, as well as number of galaxies in the center of the lens), different redshifts, and different lensing configurations (two of them, SA63 and SA80, without previously reported models). Figure 8 (first row) shows the color composite CFHT images for these four lensing groups, SL2S J08591–0345 (SA72) is the most complex, but it has the most constraints on the lens.

For the four groups quoted above, we apply a simple strong lensing mass modeling in order to estimate the Einstein radius using the LENSTOOL code (Kneib 1993; Jullo et al. 2007). Since galaxy groups are generally not well suited to performing accurate lensing models because of the lack of observational constraints (see the discussion in Limousin et al. 2009), we use a singular isothermal ellipsoid (SIE), which has only five free parameters: the position (x and y), ellipticity (e), position angle (PA), and Einstein radius. All the optimizations were done in the image plane. We want to stress that constructing detailed models for the lens is far from the scope of the present work, and the current data do not allow us to undertake such an analysis. To test more complex models more spectroscopic data is required (we are currently in a campaign to obtain this data for the arcs and galaxies in some of the SL2S groups).

SL2S J08591−0345 (SA72) at $z_l = 0.642\pm0.001$ is a confirmed galaxy group (see Muñoz et al. 2013) with three bright galaxies and two smaller ones in the center of the lens. The multiple images of this exotic lens draw an oval contour around the deflector (see top-left panel of Figure 8). The object was modeled by Orban de Xivry & Marshall (2009) as a four-component lens, showing the complexity of this compact group. In addition, the object was presented in the first sample of groups by Limousin et al. (2009), and later cataloged in the SARCS sample (More et al. 2012). Assuming that all the lensing features come from one single source at $z_s = 0.883 \pm0.001$ ($z_{phot} = 1.04\ ^{+0.04}_{-0.08}$),

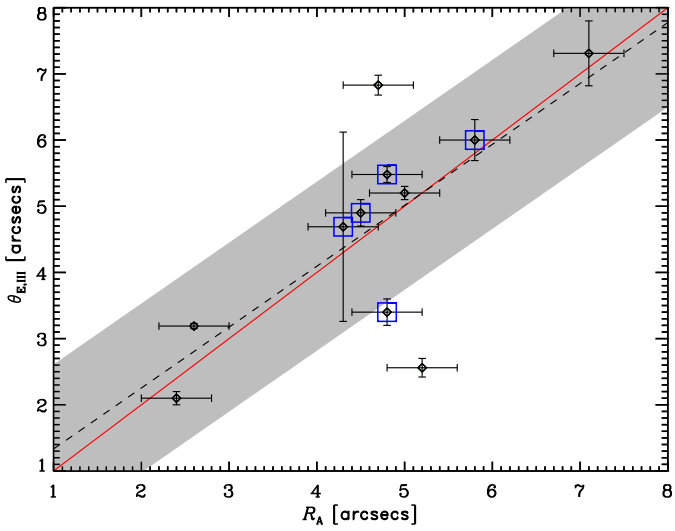

Fig. 9: The figure shows $\theta_{E,III}$ *vs* R_A for those groups with strong lensing models. The black dashed line shows the fit to the data, with the 1σ-error depicted as a gray shaded region. Blue squares are groups with giant arcs (see Section 4.1), and the red continuous line shows the one-to-one relation.

we constructed our model leaving all parameters free. Although our best model shows a large χ^2 (see Table 4), it is important to note that the complexity of a five-galaxy lens in the center of the group would require us to assume a more elaborate model than a simple SIE for its mass distribution.

SL2S J08520−0343 (SA63) is populated by two galaxies in the center (G1 and G2) and displays several arc features, with those labeled arc A and B being the most prominent (see second row, right panel of Figure 8). In the ground-based image, these arcs seems to belong to the same source, i. e., forming a system. However on the HST-ACS image this association is not so clear since arc B is brighter and straighter than arc A. Thus, to construct our model we assume arcs A and B are different systems and we used only arc A to perform the optimization. Given the resolution of the HST-ACS image, we can conjugate two points on arc A, increasing the number of constraints to six (e.g., Limousin et al. 2009; Verdugo et al. 2011). Our model predicts a demagnified counter-image for arc A (see third row, right panel of Figure 8) near galaxy G2 that can be associated with some arc-like features close to this galaxy. The results of our best fits are summarized in Table 4.

SL2S J09595+0218 (SA80) shows a configuration with two bright arcs on one side of the deflector and a very demagnified image on the other side of the deflector (see second row, left panel of the continuation of Figure 8). The photometric redshift sets the arc at $z \sim 1.2$. With only three multiple images forming the system, we have only four observational constraints. First, we set $x = 0$ and $y = 0$, leading to an elliptical mass distribution model with only three free parameters, namely, the ellipticity e, the position angle PA, and the Einstein radius. Given the impossibility of obtaining a good fit in these conditions, we proceeded in an alternative way. We set the ellipticity and the position angle with fixed values $e = 0.30$, and PA $= 30°$, leaving x and y free. In the third row and left panel of the continuation of Figure 8 we show the predicted positions of our best model, as well as the observed positions.

SL2S J10021+0211 (SA83) was discovered in the COSMOS survey (Faure et al. 2008, 2011). It has two arcs surrounding the central galaxy of the group, one long red arc (showing substructure) situated at the north (arc B) and another blue and more compact one (arc A) at the south (see second row, right panel of the continuation of Figure 8). We were able to obtain the photometric redshift only for the blue arc, z ∼ 1. Since arc A does not show surface brightness peaks that can be conjugated as different multiple image systems, there are not enough constraints to try even a simple model. However, using the position of a possible counter-image located below arc B (see second row, right panel of the continuation of Figure 8), we have two constraints, which are enough to probe the Einstein radius. Thus, following Faure et al. (2008) we perform the optimization fixing the center of the lens as the center of the bright galaxy, $e = 0.25$, and PA = 105° (see Table 1). Our model (see third row, right panel of the continuation of Figure 8) predicts that the counter-image of arc A will be very demagnified, which explains why it is not observed in the CFHT images. Our value of $\theta_{E,III}$ shown in Table 4 agrees with the value $\theta_E = 3.14''$ found by Faure et al. (2008), although our z_l and z_s values (obtained using a different methodology) are slightly different to those reported in that work.

The bottom panels of Figure 8 presents the convergence map for each strong lensing model, considering a source located at the respective redshift, z_s, given in Table 4. Dark gray lines depict the convergence locus, $\kappa = 1$, considering two different sources situated at $z_{phot} \pm \delta z_{phot}$. We note that such values are consistent with R_A (dotted blue line) and $\theta_{E,III}$ obtained from the strong lensing model (dashed blue line). In the case of SL2S J08591−0345 (SA72), the large difference between the extreme values of z_{phot} arises from the source and lens proximity in redshift.

Finally, in Figure 9 we show $\theta_{E,III}$ vs R_A for the eleven groups presented in this section. We found a good agreement between both values, with $\theta_{E,III} = (0.4 \pm 1.5) + (0.9 \pm 0.3)R_A$, a Spearman's rank correlation coefficient $R = 0.6$, and a significance $P = 6{\times}10^{-2}$. The two groups with slightly extreme values below the correlation are SA123 (SL2S J22133+0048) and SA39 (SL2S J02215−0647). This might be related to the multiple components present in their luminosity maps (see Section 5). On the other hand, the group with the value over the correlation, SA127 (SL2S J22214−0053), is a group with a high degree of elongation. We also note that the groups with giant arcs, except SA123 (SL2S J22133+0048), nearly follow the one-to-one relation.

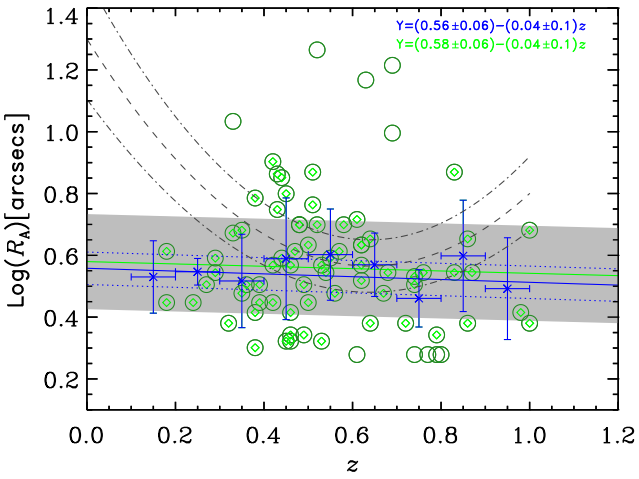

Fig. 10: The figure shows R_A as a function of the redshift. Green circles depict the secure lens candidates (Foëx et al. 2013), and green diamonds those with 2.0" ≤ R_A ≤ 8.0". Blue asterisks with error bars highlight the correlation between R_A and z after binning the data (green diamonds). The blue continuous line shows the fit to the binned data, with 1σ-error depicted as a dotted blue line. The green continuous line shows the fit to the green diamonds, with the 1σ-error depicted as a gray shaded region. The dashed line is a second-order polynomial function from Zitrin et al. (2012), assuming an error of 15% (dot-dashed line).

5. Discussion

5.1. R_A vs θ_E

In Section 4 we found a low correlation between $\theta_{E,I}$ and R_A, with a large scatter. We found $\theta_{E,I} = (2.2 \pm 0.9) + (0.7 \pm 0.2)R_A$ with a correlation coefficient $R = 0.33$, and a significance $P = 6{\times}10^{-3}$. It is important to note that the analysis was done in the whole sample (with 2.0" ≤ R_A ≤ 8.0"), without distinction between regular and irregular groups. We also note that our sample, as we commented in the introduction, does not only include giant arcs. This introduces scatter in the correlation, but even in a sample with only giant arcs, there are some groups far from the one-to-one correlation (see right column of Fig. 5). This is related to another factor that we need to consider in this comparison between $\theta_{E,I}$ and R_A, namely that we are using information at large scale (weak lensing velocity) in a lower-scale regime (strong lensing).

Gavazzi (2005) shows that departures between lensing and true mass tend to vanish at large scale. Moreover, the asphericity has a lower effect on weak lensing and X-ray-based mass estimates (see Figure 6 in Gavazzi 2005) than in the case of strong lensing. In this context, as we have measured σ_{WL} from weak lensing data (i.e. large scale), it is possible that, in some cases, we might not be able to recover the observed Einstein radius obtained when using the velocity dispersion directly in Eq. 6. Thus, at radii $\sim\theta_E$ we are probing a different mass. As we can see in the top-left panel of Fig. 5, the scatter is present in both directions, confirming this assertion. On the other hand, even if some galaxy groups look like simple lensing objects (but see Orban de Xivry & Marshall 2009; Limousin et al. 2010), they could be dynamical complex objects with multimodal components and substructures (e.g. Hou et al. 2009, 2012; Ribeiro et al. 2013). Some of our groups have luminous morphologies (Foëx et al. 2013) that cannot be associated with regular groups (roughly circular isophotes around the strong lensing system) and have elongated (elliptical isophotes with a roughly constant position angle form inner to outer parts) or multimodal morphologies (two or more peaks in the central part of the map). Since an irregular luminous morphology it is not a robust confirmation of the dynamical irregularity of a group (although the spectroscopic analysis of the seven objects in Muñoz et al. 2013 is consistent with the luminous morphology presented in Foëx et al. 2013), we carry out our analysis using groups with both irregular and regular luminous morphology. Moreover, as mentioned in Section 4.1, if we discard objects with extreme $R_A/\theta_{E,I}$ (for example with a cut off $0.5 \leq R_A/\theta_{E,I} \leq 2.0$), the correlation coefficient and the significance improve ($R = 0.6$, and $P = 1{\times}10^{-5}$). This is consistent with the idea presented above about the comparison between strong lensing mass and weak lensing mass, and is also consistent with the

results found when we used the eleven strong lensing models (Section 4.3). For such groups with extreme ratios it is more inaccurate to associate the mass at large scale with the mass inside the Einstein radius.

The velocity dispersion σ_{WL} is transformed into the corresponding mass and used to compute $\theta_{E,II}$ through Eq. (14). As before, this mass comes from a large-scale measurement, and is probably overestimated (Muñoz et al. 2013) or underestimated (Gavazzi 2005), and so it could be inappropriate to link R_A and $\theta_{E,II}$ for some groups. We note that the behavior of the points on the top-left panel of Fig. 5 are inherited by the middle-left and bottom-left panels of the same figure, with an increase in the scatter and a shift to lower values of the Einstein radius. The trend is almost the same, independently of whether we use the catalog constructed using $V_{\rm rms}$ as proxy for the velocity dispersion inferred in the observed lenses, or the one built to match the observational shape of the redshift distribution of the lenses. This is an expected result because both quantities ($\theta_{E,I}$ and $\theta_{E,II}$) are correlated through Eq. (16). Both the shift and the scatter are related to the assumed mass, M_{200}, derived from the velocity dispersion of the isothermal profile; as the mass grows without a boundary at large radii, this produces less concentrated halos, product of the $c - V_{\rm rms}$ relation. The small values of $\theta_{E,II}$ can be interpreted as a failure of ΛCDM to reproduce the observed Einstein radius (e.g., Broadhurst & Barkana 2008), but this implication is ruled out in our case considering that our analysis has oversimplifications, the most important being the assumption of spherical symmetry. Thus, consistent with the first result discussed above, we found a low correlation between $\theta_{E,II}$ and R_A. We obtained $\theta_{E,II} = (0.4 \pm 1.5) + (1.1 \pm 0.4)R_A$ with a correlation coefficient $R = 0.4$ ($P = 1{\times}10^{-3}$), and $\theta_{E,II} = (0.4 \pm 1.5) + (1.1 \pm 0.4)R_A$ with $R = 0.4$ ($P = 1{\times}10^{-3}$) for the first and second catalog, respectively.

Furthermore, the two bottom plots in the right panel of Fig. 5 show the same behavior in the correlation: statistically $\theta_{E,II}$ is slightly larger than R_A. The same behavior occurs for small values of R_A for $\theta_{E,I}$ (see top-left panel of Fig. 5). This trend is probably related to the fact that our sample does not only contain giant arcs. For instance, it is possible that some images do not form at the tips of the critical lines, which biases the comparison. However, this factor probably has less influence than the one discussed before, namely, the fact that we are using the information at large scale to infer the Einstein radius. This assertion will be clear below, when we discuss the third method.

The analysis of our strong lensing models for SL2S J08591–0345 (SA63), SL2S J08520–0343 (SA72), SL2S J09595+0218 (SA80), and SL2S J10021+0211 (SA83), and the models previously reported by Limousin et al. (2009) show that R_A can be used as a proxy of θ_E, which is quantitatively supported by the fit: $\theta_{E,III} = (0.4 \pm 1.5) + (0.9 \pm 0.3)R_A$ with a correlation coefficient $R = 0.6$. In Figure 9 we can see that the one-to-one relation is not only followed by those groups strictly defined as having giant arcs. If we compare this figure with the right column of Fig. 5, we see that groups with giant arcs are only near the one-to-one relation if we take into account the big error bars in $\theta_{E,I}$ and $\theta_{E,II}$. The fact that in our third method we found a better correlation (with less scatter) between $\theta_{E,III}$ and R_A is explained because we are using the arc positions in the models, i.e. even using simple SIE models we are directly constraining the mass inside the Einstein radius. Unfortunately, we cannot improve our statistics because we do not have enough data to perform such strong lensing models for more groups in our sample. Thus, we can regard the first and second method as a complementary study despite their lower robustness.

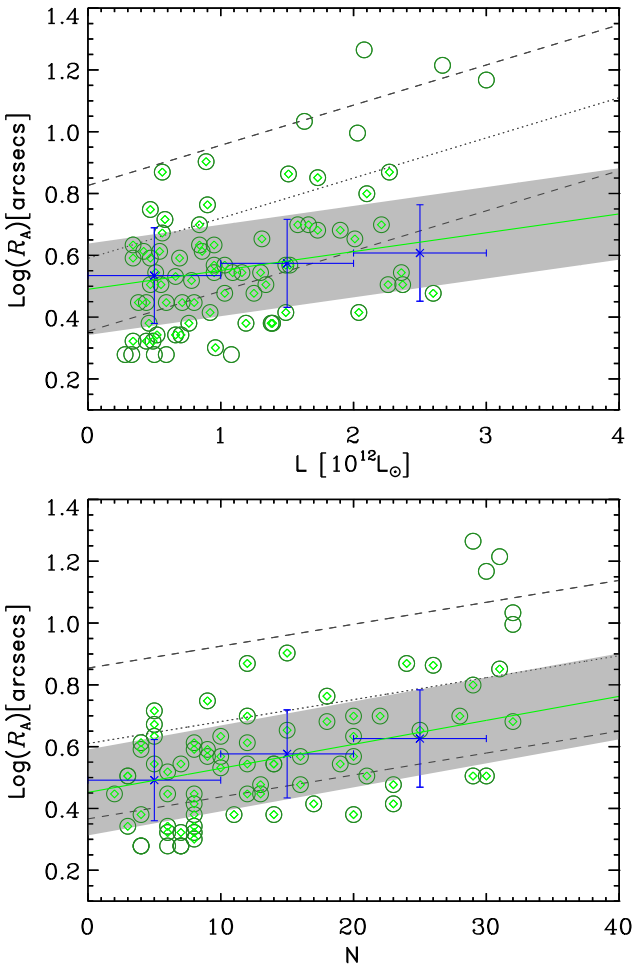

Fig. 11: *Top panel*: R_A as a function of the luminosity. Green circles depict the secure group candidates in Foëx et al. (2013), green diamonds those with 2.0" ≤ R_A ≤ 8.0". *Bottom panel*: R_A as a function of optical richness. The quantities were measured within an aperture of 0.5 Mpc. The green continuous line shows the fit to the green diamonds, with the 1σ-error depicted as a gray shaded region. Blue asterisks with error bars are plotted to highlight the correlation between R_A and luminosity or optical richness after binning the data. The dotted line shows the relations reported by Zitrin et al. (2012) with a dispersion depicted by the two dashed lines (see Sect. 5.2).

In Appendix A we present the luminosity density contours for the four new groups modeled in the present work. These contours were obtained using luminosity maps constructed following Limousin et al. (2009) and Foëx et al. (2013). From Figures A.1, A.2, and A.3 it is clear that SL2S J08591–0345 (SA63), SL2S J08520–0343 (SA72), and SL2S J09595+0218 (SA80) are regular groups with circular isophotes around the strong lensing deflector. The fourth group, SL2S J10021+0211 (SA83), has a weak-lensing detection less than 3σ, thus it is not part of the final sample of Foëx et al. (2013) and it does not appear in Fig. 5. However, this object is a good candidate to be a strong lensing group in More et al. (2012). This group also shows very elongated and elliptical isophotes, with multimodal peaks (see Fig. A.4). It is probably part of a large-scale structure, since a group or cluster is clearly present at a distance of less than 1 Mpc. There are some other examples of potentially

Table 5: Least-squares fitting results for the scaling relations

Scaling law	a ± δ a	b ± δ b	χ^2/ν	$Q(\frac{N-2}{2}, \chi^2/2)$
Log[R_A] - N	0.45 ± 0.04	0.007 ± 0.002	0.85	0.82
Log[R_A] - L	0.49 ± 0.04	0.06 ± 0.03†	0.96	0.60
Log[R_A] - (N/L)$_N$	0.44 ± 0.06	0.2 ± 0.1	0.94	0.62

Notes. (†): $\times 10^{12}$
Column (1) lists the scaling law. Columns (2) and (3) list the coefficient values in the relation $Y = a + bX$. Columns (4) and (5) list the reduced χ^2 and the statistical significance, respectively.

large-scale structures (Foëx et al. in preparation) in the sample of galaxy groups, which is not surprising since such structures have been reported in local large galaxy surveys (Colless et al. 2001; Pimbblet et al. 2004) or detected around massive clusters at higher redshifts (e.g., Limousin et al. 2012). Despite the complex morphology, R_A agrees with the value of θ_E computed from the strong lensing model, but as we noted in Fig. 5, and discussed before, irregular groups can have $R_A \approx \theta_E$.

Puchwein & Hilbert (2009) studied the cross-sections for giant arcs, using the Millennium simulation, and showed that the radial distribution of tangential arcs is broad and could extend out to several Einstein radii. Their results (see their Figure 10) are in agreement with the work presented here in the sense that the ratio R_A/θ_E could be in some cases greater than 4 (see Fig. 5). On the other hand, if we analyze our sample of eleven groups discussed in Section 4.3, we found $R_A/\theta_{E,III} = 1$ with a standard deviation of ≈35%. It is interesting that an analogous result is found for $R_A/\theta_{E,I}$ and $R_A/\theta_{E,II}$ when the outliers are eliminated (i.e., with a $0.5 \leq R_A/\theta_{E,I} \leq 2.0$ cutoff). It is beyond the scope of the present paper to analyze the impact on the Einstein radii of other effects such as the orientation (e.g., Hennawi et al. 2007), the substructures, or structures along the line of sight (Meneghetti et al. 2007; Puchwein & Hilbert 2009), the bias in concentration (Oguri & Blandford 2009) and the effect of galaxies in the lensing properties of the groups (Puchwein & Hilbert 2009). That investigation could be done in the future if more space-based images become available (optical and X-ray) to construct accurate lensing models, and more spectroscopic data is obtained to confirm the group candidates and add additional constraints to the models (see Limousin et al. 2013, and the discussion about multi-wavelength approaches). However, we want to point out that the inclusion of galaxy-scale halos in our models can boost the lensing efficiency, between 40% and 10% given the redshift of our groups and sources (see Puchwein & Hilbert 2009). Thus we will use the 35% of scatter calculated in our analysis as an estimate of all the aforementioned possible sources of error in the use of R_A as a proxy of θ_E and its relationship with the luminosity and richness.

5.2. R_A as a proxy

In the light of the above discussion, we assume that statistically R_A can be used as a proxy of the Einstein radius, especially if the Einstein radius is estimated through lens modeling and not indirectly, as in the first two methods discussed in this paper. Thus we can employ it to study some properties in galaxy groups.

5.2.1. R_A and z

As we mentioned in Section 1, Zitrin et al. (2012) found a possible Einstein radius evolution with redshift. In Fig. 10 we depicted Log(R_A) as a function of the redshift. It is evident that, if we restrict the analysis to lenses with $2.0" \leq R_A \leq 8.0"$, it is difficult to conclude the existence of an evolution of R_A with redshift, since our sample has few groups below $z = 0.2$. However, there is a trend showing a weak anti-correlation between R_A and z, which partially supports the preliminary results of Zitrin et al. (2012), i.e. galaxy groups (as clusters) are expected to be more concentrated at lower redshifts (see Sect. 3). We note that we cannot extend our conclusions to the cluster regime because of the low number of massive groups in our sample. However, if we consider as massive groups those with $R_A > 8"$, a slight increment is present in R_A for $z > 0.4$, agreeing again with Zitrin et al. (2012). For the binned data, we obtained a weak anti-correlation between R_A and z; with LogR_A = (0.56±0.06) - (0.04±0.1)z. Similarly, for the un-binned data we found LogR_A = (0.58±0.06) - (0.04±0.1)z. In both cases, the Spearman's rank correlation coefficient was ∼ 0.1, but such weak statistical dependence between the two variables is probably a result of assuming R_A as a linear function of z. As our sample is poor below $z = 0.3$, we do not attempt to perform a second-order polynomial fitting like the one in Zitrin et al. (2012). In spite of this, it is important to point out the good agreement between their second-order polynomial fitting and the present work around redshift 0.5.

Considering that the background sources have a wide range of redshifts (within each bin on redshift of the groups), we can quantify the contribution of this geometrical effect in the scatter in Fig. 10. Lets consider a fixed mass for the lens in Eq. 6, $R_A \propto D_{LS}/D_{OS}$. Taking a bin centered at $z = 0.45$ (i.e., setting $z_l = 0.45$) we found ΔLogR_A = 0.07, using the maximum and minimum z_s values for the arcs included in that bin. Therefore, the geometrical effect, estimated through ΔLogR_A, is considerably less than the dispersion observed in LogR_A (less than the 1σ-error on the correlation). Similar or even smaller values for ΔLogR_A are found if we use the other bins, indicating that this effect is negligible.

5.2.2. R_A, luminosity and richness.

The top and bottom panels in Fig. 11 show R_A as a function of luminosity and optical richness, respectively. Both parameters were measured at 0.5 Mpc from the center (see the discussion in Foëx et al. 2013). The correlations depicted in Fig. 11 are consistent with the results presented in Foëx et al. (2013). The same trends in richness and luminosity were discussed in Zitrin et al. (2012). Nevertheless, we want to stress the main differences be-

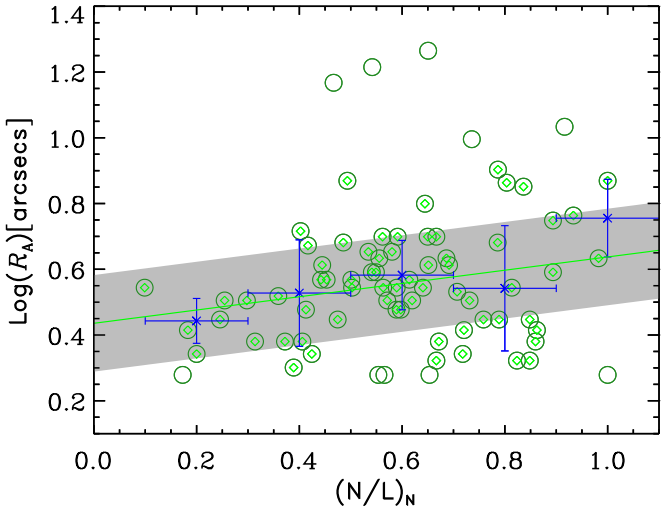

Fig. 12: R_A as a function of the (N/L)$_N$ ratio (see Sect. 5.2). Green circles depict the secure group candidates in Foëx et al. (2013), green diamonds those with 2.0" $\leq R_A \leq$ 8.0". The green continuous line shows the fit to the green diamonds, with the 1σ-error depicted as a gray shaded region. Blue asterisks with error bars represent the binned data.

tween both works. First, we are presenting the analysis in a sample of galaxy groups. Although the mass regime is included in Zitrin et al. (2012), we have a smaller limit than their lower limit of eight members (this limit set by Hao et al. 2010, since their catalog includes clusters with at least this number of members within 0.5 Mpc). Second, our groups are a bona fide sample of strong lensing groups (in some cases confirmed through spectroscopy, Thanjavur et al. 2010; Muñoz et al. 2013). In Fig. 11 we also depicted the correlations reported by Zitrin et al. (2012, see their Figure 13), taking into account the 1-σ width in the distribution. Our results are in good agreement with their work in particular for Log[R_A] - N. In the case of Log[R_A] - L our correlation is slightly shallower, possibly reflecting the different mass regime being analyzed; i.e. our sample has a cutoff at R_A = 8.0". This cutoff is more noticeable in luminosity because for massive groups we probably miss some luminous members when using a 0.5 Mpc radius.

Estimating the error in using R_A as a proxy of θ_E is complicated because R_A is measured directly from the images (see More et al. 2012), in contrast to θ_E which is estimated through modeling. Additionally, we need to consider the wide distance between the positions of the tangential arcs, i.e R_A, and the Einstein radius, produced by substructures or structures along the line of sight, the bias in concentration, or orientation effects (Hennawi et al. 2007; Meneghetti et al. 2007; Puchwein & Hilbert 2009; Oguri & Blandford 2009). Thus, we choose a 35% error (see section 5.1) in order to encompass the influence of such factors. This uncertainty on the Einstein radii is less conservative than the 25% imposed by Auger et al. (2013) in their analysis of strong gravitational lens candidates. The errors are omitted in Fig. 11 for clarity. In Table 5 we present the least-squares fitting results for both scaling relations, Log[R_A] - N and Log[R_A] - L. We also calculate the statistical significance of the fit through the $Q[(N-2)/2, \chi^2/2]$ value. Although the probability is high, indicating a strong correlation, it is important to stress the potential overestimation of errors.

As R_A correlates with N and L, it is natural to infer some dependence between R_A and the ratio N/L. Figure 12 shows Log[R_A] as a function of (N/L)$_N$, i.e. the optical richness-to-light ratio, normalized to the largest value. Table 5 show the results for our fit. Because a mass-richness relationship is found in galaxy clusters (e.g., Gladders et al. 2007; Rozo et al. 2009; Giodini et al. 2013, and references therein), we expect a correlation between N/L and the mass-to-light ratio (M/L), and thus a dependence between R_A and N/L, since the Einstein radius correlates with its enclosed mass. In particular, our group sample show R_A scale with the mass-to-light ratio (Foëx et al. in preparation). However, going beyond such connections, we want to understand the physical meaning of this correlation. Big groups, i.e. those with larger R_A, have a higher N/L ratio probably because they are less dynamically evolved (without enough time to build big galaxies), they are not relaxed, and they exhibit substructure. Thus, these groups are strong lenses, which means a large R_A. At the other end of the correlation, in small groups (small R_A) the luminosity is dominated by the brightest galaxy in the group, thus the luminosity of the group is well represented by only a few galaxy members. Given the scatter, we cannot go any further in the analysis of this correlation, and we only establish our results as tentative. Nevertheless, we are able to discuss two selection effects that would bias the correlation. First, we could have groups nearer in redshift or larger with a large R_A, thus, going down to much lower luminosities in the luminosity function (LF) would increase N and decrease L. This scenario is ruled out because both N and L are estimated within a given range in absolute magnitude (the bright part of the LF) for every redshift/velocity (see Foëx et al. 2013). Second, both N and L could have significant uncertainties due to contamination by interlopers. However, L suffers more contamination than N because, for instance, a couple of bright-foreground interlopers have a large effect on L but only change N by a comparatively small amount. We cannot completely rule out this second bias effect, and it could be associated with the discrepancies between Zitrin et al. (2012) and the correlation obtained for top panel in Fig. 11.

Foëx et al. (2013) showed that it was possible to use the optical-scaling relations as reasonable mass proxies to analyze large samples of lensing galaxy groups, and to obtain cosmological constraints. They explored the relation between σ_v and the main optical properties of the SARCS sample and found good correlations, i.e. the more massive systems are richer and more luminous (despite a 35% scatter). The analysis presented here is one more step in the analysis of strong lensing galaxy groups. The correlations discussed in the preceding paragraphs demonstrate the potential of using R_A as a complementary proxy to study a sample of lensing groups. Being galaxy groups less complex than galaxy clusters from a lensing viewpoint, the R_A and the σ_v obtained from weak lensing will be important tools to characterize galaxy groups. These are valuable assets in the forthcoming era of big surveys (LSST, DES, EUCLID) since spectroscopic data for all the objects would be not always available.

6. Conclusions

We analyzed for the first time, using different approaches, the Einstein radii in a sample of objects that belongs to the SL2S (Cabanac et al. 2007; More et al. 2012) and where selected as secure group candidates in Foëx et al. (2013). The task was done using observational data, image and spectroscopy (CFHT, HST,

IMACS), and numerical simulations (`Multidark`). Our main results can be divided in two parts and summarized as follows:

– Despite the scatter, we found a correlation between R_A and the Einstein radius in galaxy groups.
  1. Using weak lensing data (Foëx et al. 2013) we show $\theta_{E,I}$ correlates with R_A with a large scatter; $\theta_{E,I} = (2.2 \pm 0.9) + (0.7 \pm 0.2)R_A$ with $R = 0.33$. However, when we eliminate extreme values (outliers) in the ratio $R_A/\theta_{E,I}$, both the correlation coefficient and the significance improve ($R = 0.6$, and $P = 1{\times}10^{-5}$). Since the distribution of tangential arcs extends beyond the Einstein radius (e.g. Puchwein & Hilbert 2009), some scatter is expected. In our sample the scatter comes mainly because we are using the information at large scale (weak lensing velocity) in a lower-scale regime (strong lensing).
  2. Using numerical simulations, we constructed two different catalogs to mimic our sample of galaxy groups. One with $V_{\rm rms}$ as proxy for the velocity dispersion measured in the observed lenses and the second one built to match the shape of the observational redshift distribution of the lenses. We found $\theta_{E,II} = (0.4 \pm 1.5) + (1.1 \pm 0.4)R_A$ with a correlation coefficient $R = 0.4$ ($P = 1{\times}10^{-3}$), and $\theta_{E,II} = (0.4 \pm 1.5) + (1.1 \pm 0.4)R_A$ with $R = 0.4$ ($P = 1{\times}10^{-3}$) for the first and second catalog, respectively. Thus, for the second method we also found a correlation between $\theta_{E,II}$ and R_A.
  3. We presented strong lensing models obtained using the LENSTOOL code for SL2S J08591–0345 (SA63), SL2S J08520-0343 (SA72), SL2S J09595+0218 (SA80), and SL2S J10021+0211 (SA83), showing that for these groups $R_A \sim \theta_{E,III}$. The first three groups have regular morphologies, while the last one exhibits a complex morphology, probably because it is part of a large-scale structure. With the information obtained from these new models, as well as the one obtained from Limousin et al. (2009), we found $\theta_{E,III} = (0.4 \pm 1.5) + (0.9 \pm 0.3)R_A$ with a correlation coefficient $R = 0.6$. This method shows more clearly that there is a correlation between θ_E and R_A. This better agreement can be explained because these models make use of arc positions, which directly constrain the mass inside the Einstein radius.

– We found that the proxy R_A is useful to characterize some properties such as luminosity and richness in galaxy groups.
  1. Analyzing LogR_A as a function of z we found LogR_A = (0.56±0.06) - (0.04±0.1)z, and LogR_A = (0.58±0.06) - (0.04±0.1)z for the binned and un-binned data, respectively. Since our sample has few groups below $z = 0.2$, we are unable to confirm the existence of an anti-correlation between R_A and z. However, using groups with $R_A > 8$", we found a slight increment in R_A for $z > 0.4$, suggesting a possible evolution of the Einstein radius with redshift in agreement with Zitrin et al. (2012).
  2. It is shown that R_A is correlated with luminosity, and richness. The more luminous and richer the group is, the larger the R_A. We found, LogR_A = (0.45±0.04) + (0.007±0.002)N and LogR_A = (0.49±0.04) + (0.06±0.03)L. This is consistent with the weak lensing analysis of our sample presented in Foëx et al. (2013), and it is an expected result given that the Einstein radius is related to the mass of those systems.
  3. We also found a possible correlation between R_A and the N/L ratio. Groups with higher N/L ratio have greater R_A. However, considering our sample might suffer from contamination effects, we emphasize these results are only tentative and require further analysis (Foëx et al. in preparation).

SL2S offers a unique sample for the study of a strong lensing effect in the galaxy-group range (Cabanac et al. 2007; Tu et al. 2009; Limousin et al. 2009, 2010; Thanjavur et al. 2010; Verdugo et al. 2011; More et al. 2012; Muñoz et al. 2013; Foëx et al. 2013). The present paper is an additional contribution to these efforts. Currently, our research team is working on different lines, such as photometric analysis of the groups members, dynamical analysis through spectroscopy, X-ray gas distribution (Gastaldello et al. 2014), large scale structure, and numerical simulations (Fernández-Trincado et al. 2014). New results will come, incrementing our understanding of lensing galaxy groups.

Acknowledgements. We thank the anonymous referee for thoughtful suggestions. The authors also acknowledge A. Jordan for giving us part of his time in Magellan to observe our targets. We thank R. Gavazzi for allowing us to use his HST reduced images. We also thank K. Vieira for helping with proofreading. T. Verdugo acknowledges support from CONACYT through grant 165365 and 203489 through the program Estancias posdoctorales y sabáticas al extranjero para la consolidación de grupos de investigación. V. Motta gratefully acknowledges support from FONDECYT through grant 1120741. G. Foëx acknowledges support from FONDECYT through grant 3120160. R.P. Muñoz acknowledges support from CONICYT CATA-BASAL and FONDECYT through grant 3130750. M. Limousin acknowledges the Centre National de la Recherche Scientifique for its support, and the Dark Cosmology Centre, funded by the Danish National Research Foundation. G.F., M.L., and V.M. also acknowledge support from ECOS-CONICYT C12U02.

References

Abazajian, K., Adelman-McCarthy, J. K., Agüeros, M. A., et al. 2003, AJ, 126, 2081
Alard, C. 2006, ArXiv Astrophysics e-prints
Andreon, S. & Hurn, M. A. 2010, MNRAS, 404, 1922
Auger, M. W., Budzynski, J. M., Belokurov, V., Koposov, S. E., & McCarthy, I. G. 2013, MNRAS, 436, 503
Balogh, M. L., McGee, S. L., Wilman, D. J., et al. 2011, MNRAS, 412, 2303
Bardeau, S., Soucail, G., Kneib, J.-P., et al. 2007, A&A, 470, 449
Bartelmann, M. 1996, A&A, 313, 697
Becker, M. R., McKay, T. A., Koester, B., et al. 2007, ApJ, 669, 905
Bertin, E. & Arnouts, S. 1996, A&AS, 117, 393
Boldrin, M., Giocoli, C., Meneghetti, M., & Moscardini, L. 2012, MNRAS, 427, 3134
Bolzonella, M., Miralles, J.-M., & Pelló, R. 2000, A&A, 363, 476
Bridle, S. L., Kneib, J.-P., Bardeau, S., & Gull, S. F. 2002, in The Shapes of Galaxies and their Dark Halos, ed. P. Natarajan, 38–46
Broadhurst, T. & Barkana, R. 2008, ArXiv e-prints, 801
Cabanac, R. A., Alard, C., Dantel-Fort, M., et al. 2007, A&A, 461, 813
Colless, M., Dalton, G., Maddox, S., et al. 2001, MNRAS, 328, 1039
Coupon, J., Ilbert, O., Kilbinger, M., et al. 2009, A&A, 500, 981
Cucciati, O., Marinoni, C., Iovino, A., et al. 2010, A&A, 520, A42
Cui, W., Springel, V., Yang, X., De Lucia, G., & Borgani, S. 2011, MNRAS, 416, 2997
Dalal, N., Holder, G., & Hennawi, J. F. 2004, ApJ, 609, 50
Eke, V. R., Baugh, C. M., Cole, S., et al. 2004, MNRAS, 348, 866
Evrard, A. E., Metzler, C. A., & Navarro, J. F. 1996, ApJ, 469, 494
Faltenbacher, A. & Mathews, W. G. 2007, MNRAS, 375, 313
Faure, C., Anguita, T., Alloin, D., et al. 2011, A&A, 529, A72+
Faure, C., Kneib, J.-P., Covone, G., et al. 2008, ApJS, 176, 19
Fernández-Trincado, J. G., Forero-Romero, J. E., Foex, G., Verdugo, T., & Motta, V. 2014, ApJ, 787, L34
Finoguenov, A., Ponman, T. J., Osmond, J. P. F., & Zimer, M. 2007, MNRAS, 374, 737
Foëx, G., Motta, V., Limousin, M., et al. 2013, A&A, 559, A105
Foëx, G., Soucail, G., Pointecouteau, E., et al. 2012, A&A, 546, A106
Gastaldello, F., Limousin, M., Foëx, G., et al. 2014, MNRAS, 442, L76
Gavazzi, R. 2005, A&A, 443, 793
Gavazzi, R., Marshall, P. J., Treu, T., & Sonnenfeld, A. 2014, ApJ, 785, 144
Gavazzi, R., Treu, T., Marshall, P. J., Brault, F., & Ruff, A. 2012, ApJ, 761, 170
Giodini, S., Lovisari, L., Pointecouteau, E., et al. 2013, Space Sci. Rev.

Gladders, M. D., Yee, H. K. C., Majumdar, S., et al. 2007, ApJ, 655, 128
Golse, G. & Kneib, J.-P. 2002, A&A, 390, 821
Gwyn, S. D. J. 2011, ArXiv e-prints
Hao, J., McKay, T. A., Koester, B. P., et al. 2010, ApJS, 191, 254
Helsdon, S. F. & Ponman, T. J. 2000a, MNRAS, 319, 933
Helsdon, S. F. & Ponman, T. J. 2000b, MNRAS, 315, 356
Hennawi, J. F., Dalal, N., Bode, P., & Ostriker, J. P. 2007, ApJ, 654, 714
Hildebrandt, H., Erben, T., Kuijken, K., et al. 2012, MNRAS, 421, 2355
Hou, A., Parker, L. C., Harris, W. E., & Wilman, D. J. 2009, ApJ, 702, 1199
Hou, A., Parker, L. C., Wilman, D. J., et al. 2012, MNRAS, 421, 3594
Jarosik, N., Bennett, C. L., Dunkley, J., et al. 2011, ApJS, 192, 14
Joseph, R., Courbin, F., Metcalf, R. B., et al. 2014, A&A, 566, A63
Jullo, E., Kneib, J.-P., Limousin, M., et al. 2007, New Journal of Physics, 9, 447
Kinney, A. L., Calzetti, D., Bohlin, R. C., et al. 1996, ApJ, 467, 38
Klypin, A., Kravtsov, A. V., Bullock, J. S., & Primack, J. R. 2001, ApJ, 554, 903
Klypin, A., Valenzuela, O., Colín, P., & Quinn, T. 2009, MNRAS, 398, 1027
Klypin, A. A., Trujillo-Gomez, S., & Primack, J. 2011, ApJ, 740, 102
Kneib, J.-P. 1993, PhD thesis, Université Paul Sabatier, Toulouse III, France
Knobel, C., Lilly, S. J., Iovino, A., et al. 2009, ApJ, 697, 1842
Komatsu, E., Dunkley, J., Nolta, M. R., et al. 2009, ApJS, 180, 330
Li, I. H., Yee, H. K. C., Hsieh, B. C., & Gladders, M. 2012, ApJ, 749, 150
Limousin, M., Cabanac, R., Gavazzi, R., et al. 2009, A&A, 502, 445
Limousin, M., Ebeling, H., Richard, J., et al. 2012, A&A, 544, A71
Limousin, M., Jullo, E., Richard, J., et al. 2010, A&A, 524, A95
Limousin, M., Morandi, A., Sereno, M., et al. 2013, Space Sci. Rev., 177, 155
Lin, Y.-T., Mohr, J. J., & Stanford, S. A. 2003, ApJ, 591, 749
LSST Dark Energy Science Collaboration. 2012, ArXiv e-prints
Mandelbaum, R., Seljak, U., Cool, R. J., et al. 2006, MNRAS, 372, 758
Marshall, P. J., Hogg, D. W., Moustakas, L. A., et al. 2009, ApJ, 694, 924
Maturi, M., Mizera, S., & Seidel, G. 2013, ArXiv e-prints
McLeod, B. A., Bernstein, G. M., Rieke, M. J., & Weedman, D. W. 1998, AJ, 115, 1377
Meneghetti, M., Argazzi, R., Pace, F., et al. 2007, A&A, 461, 25
Meneghetti, M., Bartelmann, M., Dahle, H., & Limousin, M. 2013, ArXiv e-prints
Meneghetti, M., Bartelmann, M., & Moscardini, L. 2003, MNRAS, 340, 105
Meneghetti, M. & Rasia, E. 2013, ArXiv e-prints
Miralda-Escude, J. & Babul, A. 1995, ApJ, 449, 18
More, A., Cabanac, R., More, S., et al. 2012, ApJ, 749, 38
More, A., Jahnke, K., More, S., et al. 2011, ApJ, 734, 69
Muñoz, R. P., Motta, V., Verdugo, T., et al. 2013, A&A, 552, A80
Narayan, R. & Bartelmann, M. 1996, ArXiv Astrophysics e-prints
Navarro, J. F., Frenk, C. S., & White, S. D. M. 1997, ApJ, 490, 493
Oguri, M. & Blandford, R. D. 2009, MNRAS, 392, 930
Orban de Xivry, G. & Marshall, P. 2009, MNRAS, 399, 2
Osmond, J. P. F. & Ponman, T. J. 2004, MNRAS, 350, 1511
Pimbblet, K. A., Drinkwater, M. J., & Hawkrigg, M. C. 2004, MNRAS, 354, L61
Popesso, P., Biviano, A., Böhringer, H., Romaniello, M., & Voges, W. 2005, A&A, 433, 431
Prada, F., Klypin, A. A., Cuesta, A. J., Betancort-Rijo, J. E., & Primack, J. 2012, MNRAS, 423, 3018
Puchwein, E. & Hilbert, S. 2009, MNRAS, 398, 1298
Rasmussen, J. & Ponman, T. J. 2007, MNRAS, 380, 1554
Redlich, M., Bartelmann, M., Waizmann, J.-C., & Fedeli, C. 2012, A&A, 547, A66
Reyes, R., Mandelbaum, R., Hirata, C., Bahcall, N., & Seljak, U. 2008, MNRAS, 390, 1157
Ribeiro, A. L. B., Schilling, A. C., de Carvalho, R. R., et al. 2013, ArXiv e-prints
Richard, J., Pei, L., Limousin, M., Jullo, E., & Kneib, J. P. 2009, A&A, 498, 37
Riebe, K., Partl, A. M., Enke, H., et al. 2011, ArXiv e-prints
Romeo, A. D., Napolitano, N. R., Covone, G., et al. 2008, MNRAS, 389, 13
Rozo, E., Rykoff, E. S., Evrard, A., et al. 2009, ApJ, 699, 768
Sand, D. J., Treu, T., Ellis, R. S., & Smith, G. P. 2005, ApJ, 627, 32
Seidel, G. & Bartelmann, M. 2007, A&A, 472, 341
Sommer-Larsen, J. 2006, MNRAS, 369, 958
Sun, M. 2012, New Journal of Physics, 14, 045004
Sygnet, J. F., Tu, H., Fort, B., & Gavazzi, R. 2010, A&A, 517, A25
Thanjavur, K., Crampton, D., & Willis, J. 2010, ArXiv e-prints
Torri, E., Meneghetti, M., Bartelmann, M., et al. 2004, MNRAS, 349, 476
Tu, H., Gavazzi, R., Limousin, M., et al. 2009, A&A, 501, 475
Turner, E. L., Ostriker, J. P., & Gott, III, J. R. 1984, ApJ, 284, 1
Verdugo, T., Motta, V., Muñoz, R. P., et al. 2011, A&A, 527, A124
Willis, J. P., Pacaud, F., Valtchanov, I., et al. 2005, MNRAS, 363, 675
Wilman, D. J., Balogh, M. L., Bower, R. G., et al. 2005a, MNRAS, 358, 88
Wilman, D. J., Balogh, M. L., Bower, R. G., et al. 2005b, MNRAS, 358, 71
Wright, C. O. & Brainerd, T. G. 2000, ApJ, 534, 34
Yang, X., Mo, H. J., & van den Bosch, F. C. 2008, ApJ, 676, 248
Zitrin, A., Broadhurst, T., Bartelmann, M., et al. 2012, MNRAS, 423, 2308

Appendix A: Luminosity density contours

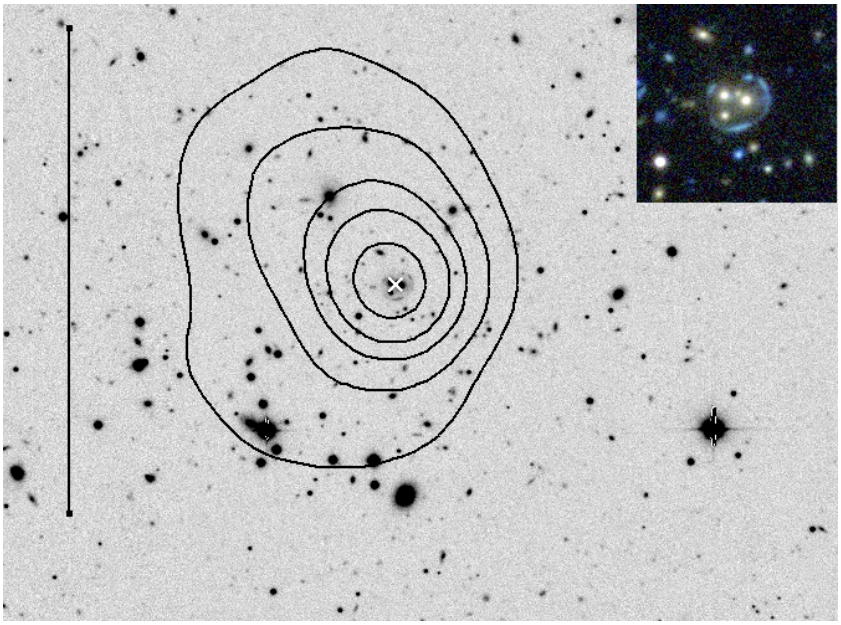

Fig. A.1: Luminosity density contours for SL2S J08591–0345 (SA63). They represent 2×10^6, 4×10^6, 7×10^6 and 10^7, and 1.5×10^7 $L_\odot\,kpc^{-2}$ from outermost to innermost. The white cross marks the galaxy at the center of the strong lensing system. The black vertical line on the left is 1 Mpc long. The stamp in the top-right corner shows a 30″×30″ CFHTLS false color image of the system.

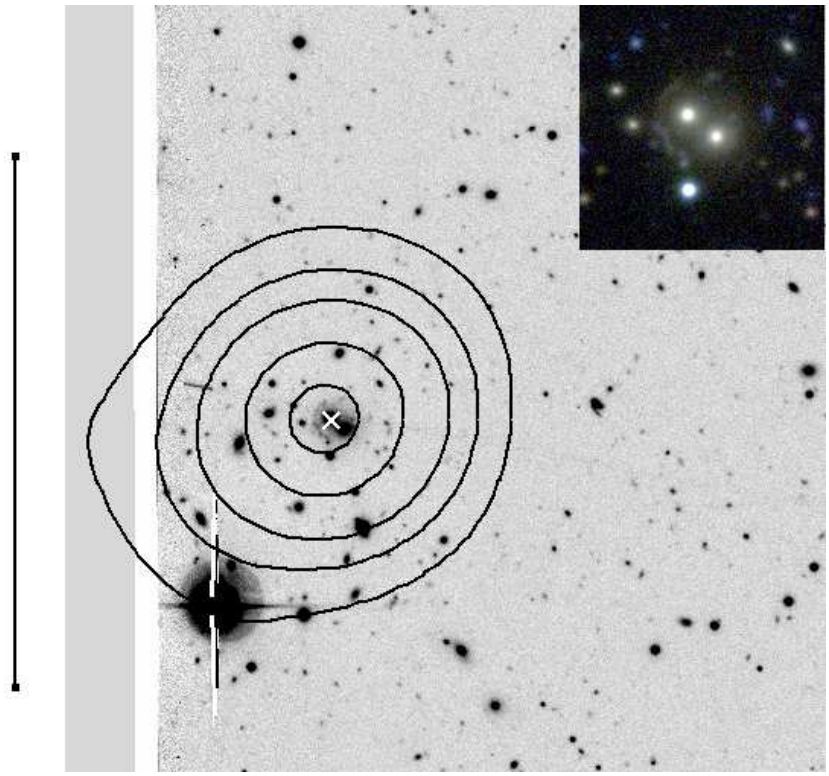

Fig. A.2: Same as Fig. A.1 for SL2S J08520–0343 (SA72)

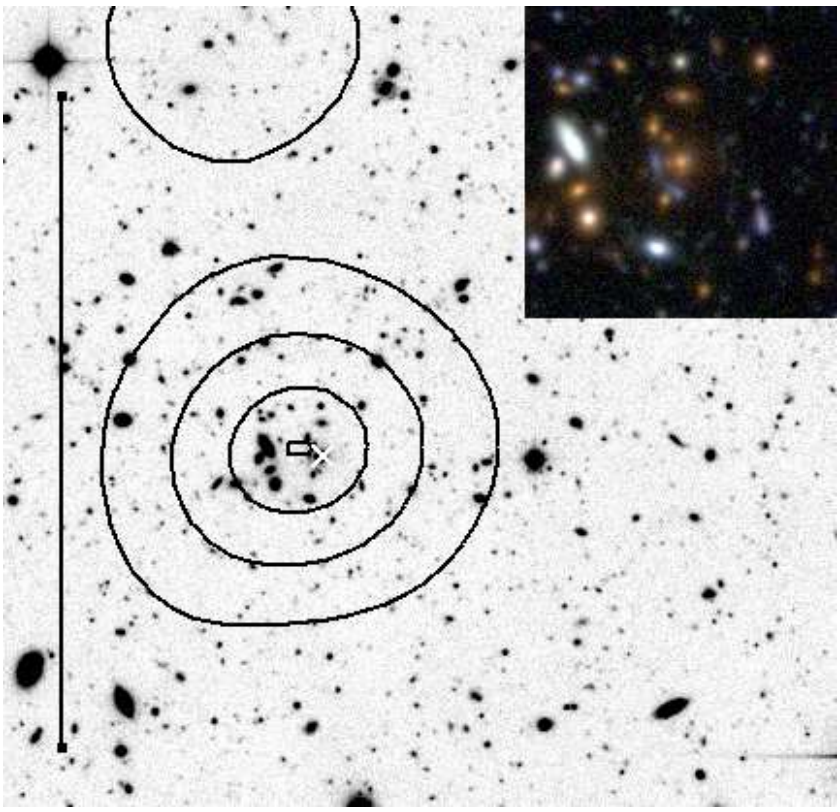

Fig. A.3: Same as Fig. A.1 for SL2S J09595+0218 (SA80).

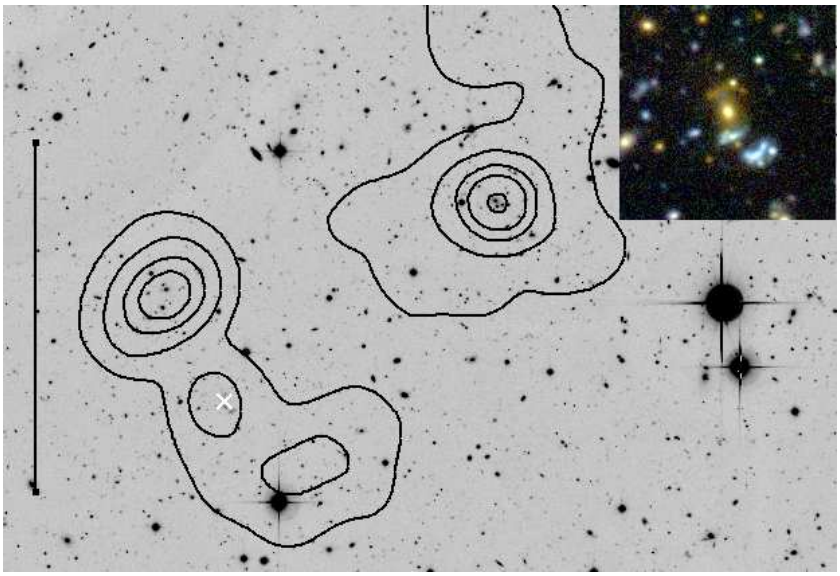

Fig. A.4: Same as Fig. A.1 for SL2S J10021+0211 (SA83).